Politecnico di Milano
Scuola di Ingegneria Industriale e dell'Informazione
Corso di Laurea Magistrale in Ingegneria Biomedica

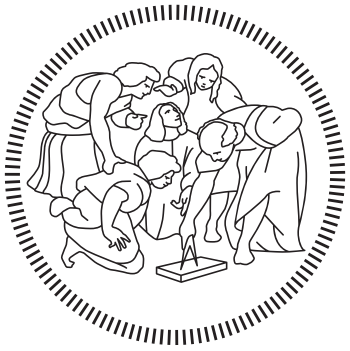

# Artery-Vein Differential Analysis of Retinal Microvasculature Features in Optical Coherence Tomography - Angiography for Diabetic Retinopathy Detection

Advisor: Prof. Enrico Gianluca Caiani

Thesis by:
Mattia CASTELNUOVO Matr. 919463

Academic Year 2020–2021

*Al fünch e a la rosa.*

# Acknowledgments

Firstly, I want to thank Prof. Enrico Caiani for his assistance during the every phase of this study.

Secondly, I want to thank Dr. Xincheng Yao of University of Illinois at Chicago and his laboratory for the opportunity to learn how to properly collect and process their data.

Thanks to my family, who always supported me, and especially my parents, who made this journey possible in the first place.

Special thanks to Giulia, whose positiveness, warmth and sincere love helped me and still help me every day.

# Contents

# List of Figures

# List of Tables

# Abbreviations

| | |
|---|---|
| DR | Diabetic Retinopathy |
| DM | Diabetes Mellitus |
| NoDR | Patients with Diabetes but not Diabetic Retinopathy |
| NPDR | Non-Proliferative Diabetic Retinopathy |
| OCT | Optical Coherence Tomography |
| OCTA | Optical Coherence Tomography - Angiography |
| VPI | Vessel Perimeter Index |
| VDI | Vessel Diameter Index |
| VSD | Vessel Skeleton Density |
| VAD | Vessel Area Density |
| VCI | Vessel Complexity Index |
| FD | Fractal Dimension |

# Abstract

Diabetic Retinopathy is a increasing source of loss of vision worldwide. Developing better knowledge bases and tools to diagnose it as early as possible is of great importance. This study aims to expand previous studies by measuring and analyzing six features on differentiated Artery-Vein OCTA vessel maps in order to help diagnose Diabetic Retinopathy in its Non-Proliferative stages. Six features (VPI, VDI, VSD,V AD, VCI and FD) have been automatically calculated on arteries and veins only and then used to derive four feature sets. The classification of the vessels was made possible by previously published algorithms. For each feature, four values have been derived (feature sets): artery value, vein values, average values and ratios between the artery and vein values. A complete statistical analysis was performed using two sets of three cohorts (Control, NoDR and NPDR and Mild, Moderate and Severe NPDR). The Bonferroni Correction was applied in order to minimize the risk of False Positives.

Insights about the illness have been gained, especially surrounding the balance between artery and vein values, which is shown to be perturbed by the onset (but not the severity) of DR. The observed results hint at a high significance of A/V Ratio measurements and of the VCI feature. A/V Ratio are shown to reach statistical significance in five out of the six features, and are also able to differentiate the NPDR cohort from both the others in two of the six features.

# Chapter 1

# Background

## 1.1 Diabetic Retinopathy

### 1.1.1 A Global Cause for Concern?

Diabetic Retinopathy (DR) is a pathology that belongs to the wider family of retinopathies. As the name implies, this illness affects the retina of patients with Diabetes Mellitus (DM). It is estimated that, for US citizens aged 20 to 64, DR is the leading cause of blindness [1]. A study from 2004 estimated that the number of Americans affected by DR is greater than 4 million [2]. The study also observed that four out of ten DM patients aged 40+ develop DR. Taking a look at the global situation, in 2018 Pandey et al cast a prediction for 2025 [3]. By that year, the predicted number of people affected by diabetes-related retinopathies in the world will almost reach 600 million. Since the endpoint of DR is blindness, even before the Covid19 pandemic, this increase in affected patients can likely cause strain on the healthcare systems, especially the ones of countries with a high diabetic population and the ones of developing countries. An early diagnose of Diabetic Retinopathy is crucial: an early detection is able to prevent, at least partially, the loss of vision caused by DR [3]. Diagnosing the first stages of DR will bring many benefits to the patients and to the healthcare providers.

### 1.1.2 Onset and Progression

Diabetes Mellitus, which is a necessary but not sufficient condition to develop DR, has the effect of increasing the glucose concentration in the blood stream. This can lead to blockages in the retina blood vessels. When this happens, the blood flow is impeded and the vessel walls can break. This first stage is called NPDR (Non-Proliferative DR), as no new vessels are formed to replace the (even partially) blocked ones. The leakings have the effect of swelling the eye and the retina, which in turn increase the number and severity of the leakings. When many vessels become completely blocked, the severity of Diabetic Retinopathy increases

and a new stage is reached. The stage of PDR (Proliferative DR) is named so because new blood vessels begin to be formed. However, these vessels are not formed properly and the leakings are not only unavoidable, but also increased. All of these leaks will gradually increase the pressure in the eye. The greater pressure cannot be endured by the optic nerve fibers, which become more and more damaged. As a consequence, there will be a mounting loss of vision. Another consequence is that the retina may start to detach. The loss of vision is permanent even if stopped. Thus, an early diagnosis can prevent permanent damage in the an important sensory organ in the human body. A diagnosis of DR in its NPDR stage will reduce vision damage to the minimum. Figure 1.1 shows a comparison between an Healthy eye and an eye with Severe NPDR.

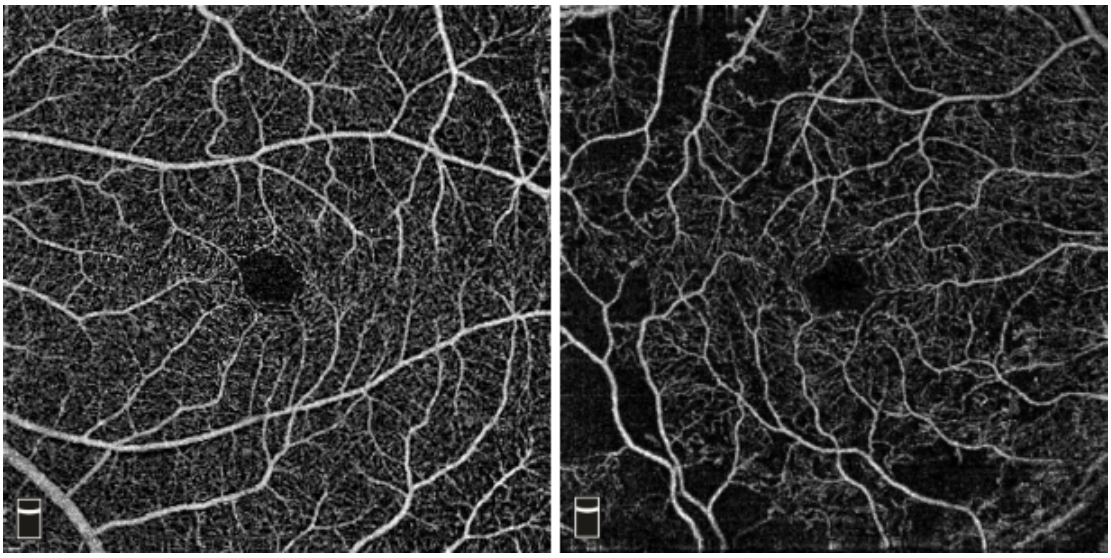

Figure 1.1: OCTA images of a Healthy eye (left) and a Severe NPDR eye (right) from two different patients. Adapted from *Differential Artery-Vein Analysis in OCT Angiography of Diabetic Retinopathy* [9], 2021, Copyright 2021 by UIC.

## 1.2 DR Biomarkers in Blood Vessels

The problem of oxygen transport and blood flow was studied by Murray in 1926 [4]. The base for his reasoning was the hypothesis of maximum energetic economy of the blood flow. As a consequence, blood vessels should have some kind of preferred physiological patterns in terms of radius, number, branching, etc. Oxygen flow through the cardiovascular system is impaired whenever the vessels deviate from the physiological standards. Ernest et al. observed in 1983 that hyperglycemia in dogs impaired oxygen autoregulation [5]. Grunwald et al. found in 1996 that Diabetes Mellitus increased total volumetric blood flow rate and "decreased regulatory responses to hyperoxia" [6]. Total volumetric blood flow rate increased

along with the illness duration. With the introduction of advances in digital imaging, the number and the quality of studies in this field has increased. Sasongko et al. performed a study on 1159 subjects in 2010 [7]. They observed a correlation between Diabetes Mellitus (and Diabetic Retinopathy) and an abnormal pattern of blood vessels: "Longer diabetes duration was associated with larger arteriolar branching angle and increased arteriolar [tortuosity]". Also, hyperglycemia was also associated with increased arteriolar tortuosity. Some of these changes occur even before that DR begins to develop in the patient.

## 1.3 Fundus Images

Fundus Imaging was invented almost a century ago, but its use increased and widened with the arrival of digital imaging, which offered major improvements in image acquisition and analysis. "Fundus" refers to the "Fundus Oculi" (Latin for "back of the eye"), which is the retina. Fundus images are taken with a Fundus Camera, a special kind of camera which illuminates the retina and captures its reflected light [8]. Both of these actions are performed through the pupil, which acts as "both entrance and exit for its illuminating and imaging light rays" [9]. As can be seen in Figure 1.2, the macula (center), the optic disk (center left) and the major blood vessels can be distinguished. It can be also noted that the image was captured using RGB channels, having thus three signals per pixels. These signals can be used to extract color-sensitive information [10]. Specific fluorescent dyes can be used to enhance the contrast of certain parts of the image, improving the identification and segmentation of specific areas.

These characteristics made Fundus imaging the traditional method to "follow, diagnose and treat eye diseases" [8]. This includes the identification of Diabetic Retinopathy. A number of studies have been performed to diagnose DR (automatically or not) by segmenting blood vessels and/or by searching for and locating specific lesions in the retina [11]. Specific procedures have been implemented to locate microaneurysms and small hemorrhages, which are clues that point to blood circulation abnormalities. Some of these algorithms (using Deep Learning models) managed to reach an AUC (Area Under the Curve) of 0.99. Similarly successful were the attempts of using Convolutional Neural Networks to segment and analyze blood vessels and their pattern, reaching over 97 % accuracy. There are disadvantages to these approaches, namely the fact that the inner workings of the models are not humanly intelligible, thus requiring lots of time and effort in case of errors or unexpected behaviors. There have also been attempts of manual measurements used for the same purpose. E.g. in 2014, Habib et al. manually measured six geometric features to see whether their distributions were statistically different in Control, NPDR and DR patients [12]. Moreover, the presence of lesions in the retina makes recognising the blood vessels near them difficult, and the image quality may vary depending on many factors. Nonetheless, there seem

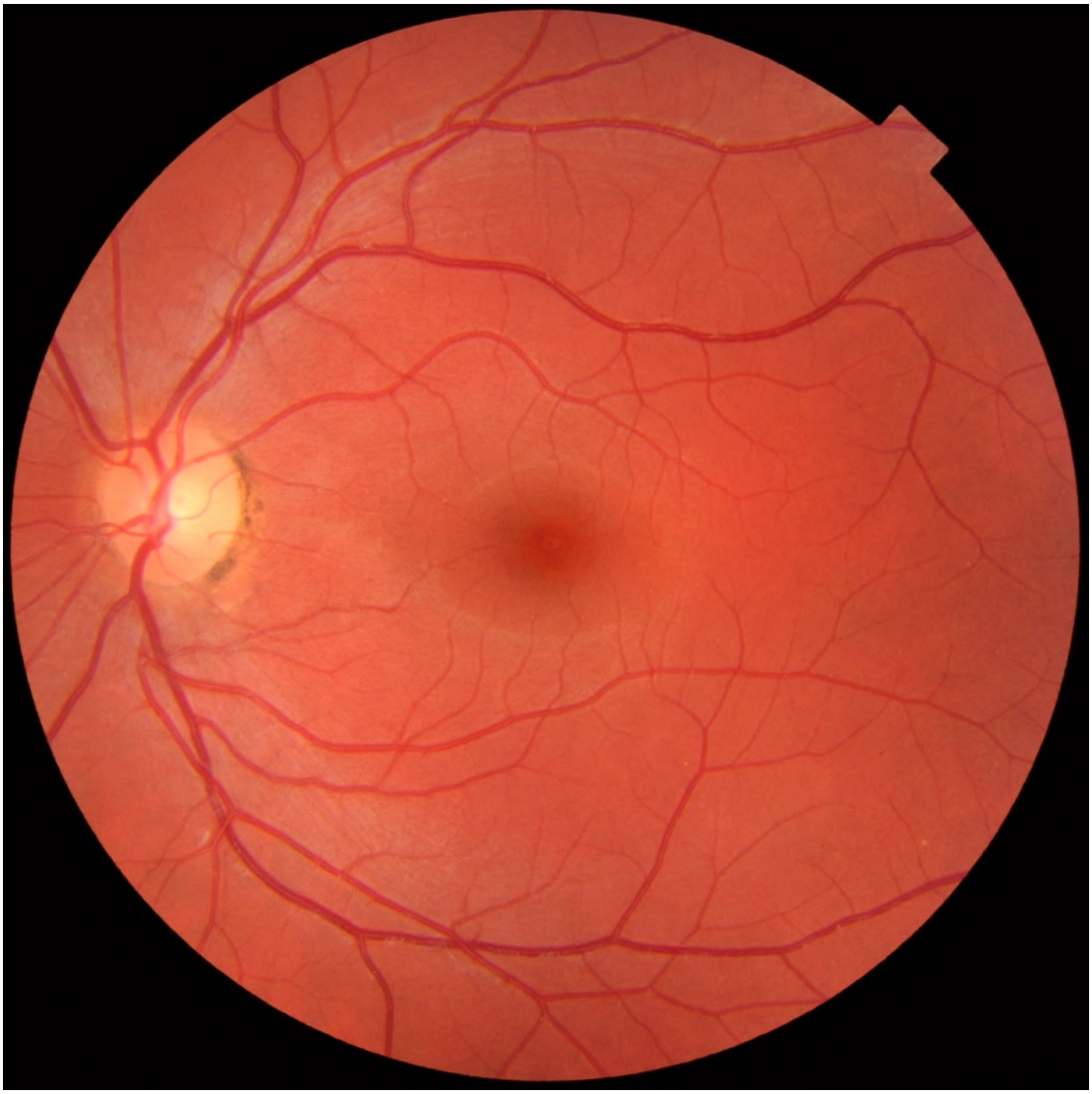

Figure 1.2: Fundus Image of the left eye of a healthy 25 Swedish years old male. By Mikael Häggström, used with permission.

to be promising results.

## 1.4 Optical Coherence Tomography-Angiography (OCTA)

Optical Coherence Tomography-Angiography (OCTA) is an imaging technique that is noncontact and noninvasive. Its output is a tridimensional image composed of multiple monochromatic bidimensional scans which can differentiate between blood vessels and background tissues. In the last twenty years, its "speed, acquisi-

tion speed and resolution" underwent major improvements [13]. "Its noninvasive and tridimensional nature makes it preferable to invasive and bidimensional methods such as Fluorescein Angiography (FA)" [9]. As a result of that, this technique achieved "rapid and wide adoption in ophthalmology" [13]. Moreover, a number of solutions exist in order to increase OCTA blood vessel contrast. Figure 1.3 shows how OCTA enhances the smaller vessels barely visible (or not visible at all) in the En Face OCT image.

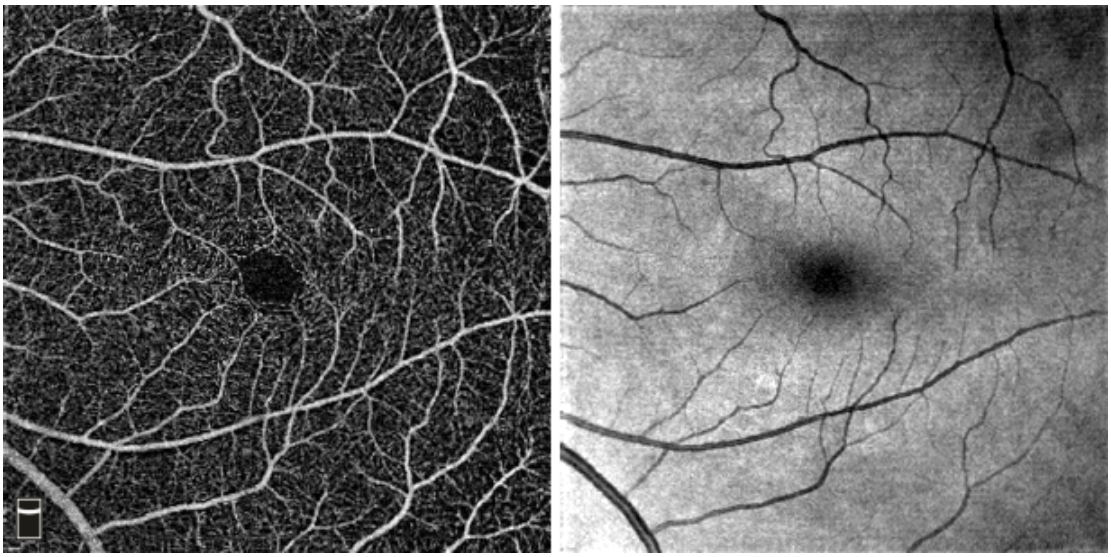

Figure 1.3: En-Face OCT image (left) and corresponding OCTA image (right) of a Healthy eye. Adapted from *Differential Artery-Vein Analysis in OCT Angiography of Diabetic Retinopathy* [9], 2021, Copyright 2021 by UIC.

OCTA images have been used to identify vessel geometry and blood flow abnormalities [14, 15]. The popularity of this method also means that it has been used to identify different retinopathies, such as:

- Age-Related Macular Degeneration [16–20];
- Sickle Cell Retinopathy [21–24];
- Diabetic Retinopathy [9, 25–41].

Regarding the identification of DR, many features have been proposed and studied over the years In this study, six of such features will be measured and analyzed. However, unlike previous studies, these features are going to be measured two times: on arteries only and on veins only. From these two measurements, four feature sets will be derived and analyzed. In order to do this, arteries and vein have to be differentiated from each other.

## 1.5 Differentiation of Arteries and Veins

Artery-Vein differentiation has previously been used to search for increased sensitivity in diagnosing DR and its stages and also to observe if and how the illness affected arteries or veins in a different way [9]. In 2019, Alam et al. demonstrated that measuring features on arteries and veins separately increased sensitivity on Sickle Cell retinopathy identification [22].

There many strategies that have been proposed to classify the vessels in different types of images, like the mentioned Fundus [10, 42] and OCTA images. For the latter, such methods range from Near Infrared Oxymetry [43] to Deep Learning models [44]. In this study, the process to differentiate arteries from veins is the same as the work by Castelnuovo [9], which is a slight modification of the algorithm developed by Alam et al. in 2019 [45].

## 1.6 Definitions of DR Stages

In this study, all the patients affected by Diabetic Retinopathy were diagnosed with different stages of NPDR. There are no PDR patients' images. Non-Proliferative Diabetic Retinopathy is divided into three stages (Mild, Moderate and Severe) defined by the American Diabetes Association (ADA) like follows [46] :

- Mild NPDR: "Small areas of balloon-like swelling in the retina's tiny blood vessels, called microaneurysms, occur at this earliest stage of the disease. These microaneurysms may leak fluid into the retina". This stage of the illness is the very first one, and is the ideal one to be differentiated from the cohorts that present no retinopathy;
- Moderate NPDR: "As the disease progresses, blood vessels that nourish the retina may swell and distort. They may also lose their ability to transport blood. Both conditions cause characteristic changes to the appearance of the retina and may contribute to DM". This stage is sort of a middle point between the start of the illness and its more damaging stages;
- Severe NPDR: "Many more blood vessels are blocked, depriving blood supply to areas of the retina. These areas secrete growth factors that signal the retina to grow new blood vessels". This is the stage immediately preceding the Proliferative phase of the illness (PDR).

## 1.7 Aims

The aim of this study is to test whether measuring six selected features on differentiated Artery-Vein OCTA vessel maps can increase the sensitivity of Diabetic Retinopathy detection in its Non-Proliferative stages.

# Chapter 2

# Materials and Methods

This study follows the ethical standards contained in the Declaration of Helsinki by the World Medical Association.

## 2.1 Composition of the Dataset

A total of 143 OCTA images of both right and left eyes of patients, belonging to five cohorts, were used for this study. All of these images are macular scans taken by the Lions of Illinois Eye Research Institute (LIERI) using an ANGIOVUE® spectral domain OCTA system (Optovue, Fremont, CA) with a 70-kHz A-scan rate, an axial resolution of 5 µm, and a lateral resolution of 15 µm. The images were exported by the ReVue® software (Optovue, Fremont, CA). The dataset is a slightly expanded version of the one used in the work by Castelnuovo [9]. A total of four images were added to that dataset. Every image has a different quality score assigned to it by the software, which is taken into account when choosing which images to add to the dataset. The staging of the illness in the images was done by a specialized professional. The five cohorts that will be used in this study are composed by:

- 32 images belonging to Control patients (without both Diabetes and Diabetic Retinopathy);
- 24 images belonging to NoDR patients (with Diabetes but without Diabetic Retinopathy);
- 24 images belonging to Mild NPDR patients;
- 22 images belonging to Moderate NPDR patients;
- 41 images belonging to Severe NPDR patients.

## 2.2 Obtaining a Binary Vessel Map from the Raw OCTA Image

Since OCTA images are tri-dimensional volumes made of bi-dimensional scans, the very first step is to extract a single level from the mesh. The "Outer Retina" level was selected for all images in the dataset. The extracted images were processed by a custom-made Matlab® (Mathworks, Natick, MA) scripts.

Firstly, the images are filtered with a Frangi 2D filter. This filter enhances the edges of the blood vessels. Secondly, the resulting images are binarized using a single threshold, slightly different for every image in order to have the best output quality. Thirdly, spurious pixels are eliminated and small holes in the vessels are filled. Also, small unconnected clusters of pixels are also cleaned. This step concludes the preprocessing of the images. The complete procedure is shown in Figure 2.1. Figure 2.2 shows the input and the output images of the preprocessing step.

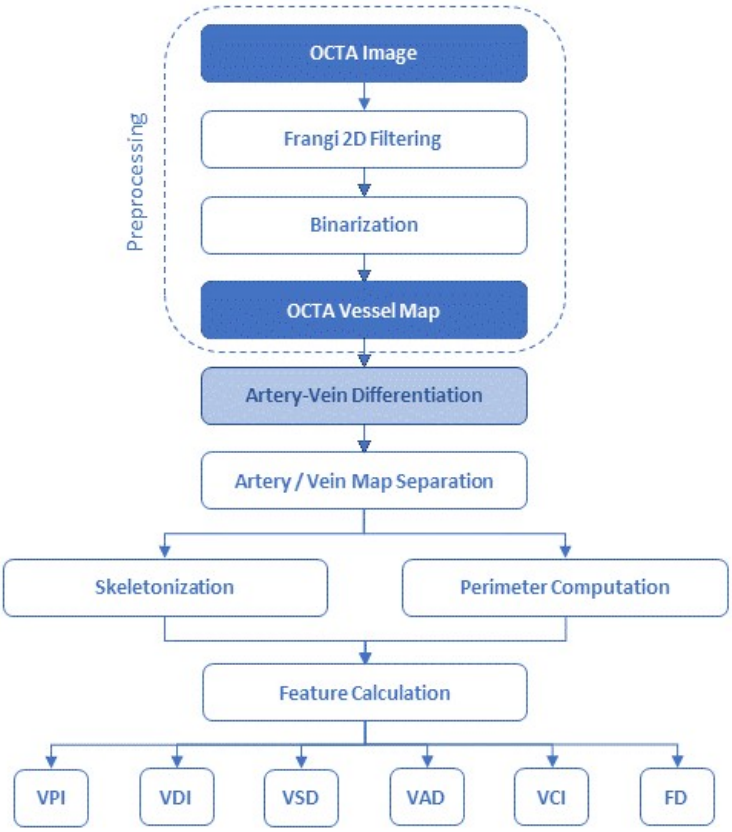


Figure 2.1: Simple flowchart showing all main steps of this study from the raw OCTA image to the six measured features

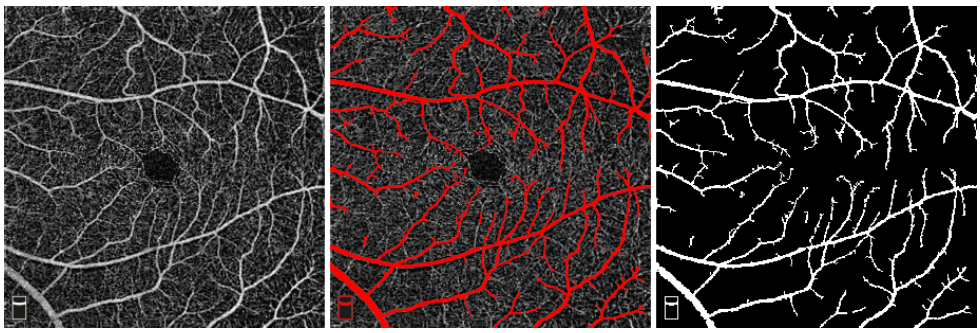

Figure 2.2: Overview of the preprocessing step. Left: raw OCTA image. Right: output binary vessel map. Center: overlay of the vessel map (red) on the OCTA image in order to assess the "goodness" of the preprocessing steps. Adapted from *Differential Artery-Vein Analysis in OCT Angiography of Diabetic Retinopathy* [9], 2021, Copyright 2021 by UIC.

## 2.3 Differentiating Arteries from Veins

This algorithm, developed by Alam et al [45] in 2019, is able to differentiate arteries from veins using OCT images. While the original workflow took as input En Face OCT images, in this study both En Face and Outer Layer OCT images will be used, following the procedure shown in [9]. The rationale for using the OCT images for this classification is that, since "the en face OCT and OCTA are naturally reconstructed from the same spectrogram data sets, the OCT artery-vein vessel map can be readily used to guide artery-vein differentiation in corresponding OCTA" [45]. This procedure is illustrated in Figure 2.3. It can be seen that Outer Layer OCT images are used only to obtain a vessel mask, while the En Face OCT images are used for the proper artery-vein differentiation. Figure 2.4 shows the Source Node Classification step more in detail.

### 2.3.1 Bias Field Correction

OCT images tend to suffer from intensity dis-homogeneity [45]. In order to eliminate this undesirable condition, a Bias Field Correction step has to be added to the image preprocessing. The workflow is straightforward. Firstly, the bias field of the image is estimated. The image is modeled as the result of the pixel-by-pixel product of the "true" image and the bias field. The bias field is then modeled as the weighted sum of smooth basis functions. "20 polynomials of the first degree are chosen as the basis functions" [45]. This leaves only the weights of these functions to be estimated. Secondly, according to the chosen model, the image is divided by the estimated bias field. This Correction is applied to both the En Face and the Outer Layer OCT, as shown in Figure 2.3. Figure 2.5 and Figure 2.6 shows the preprocessing steps applied to both En Face and Outer Layer OCT images.

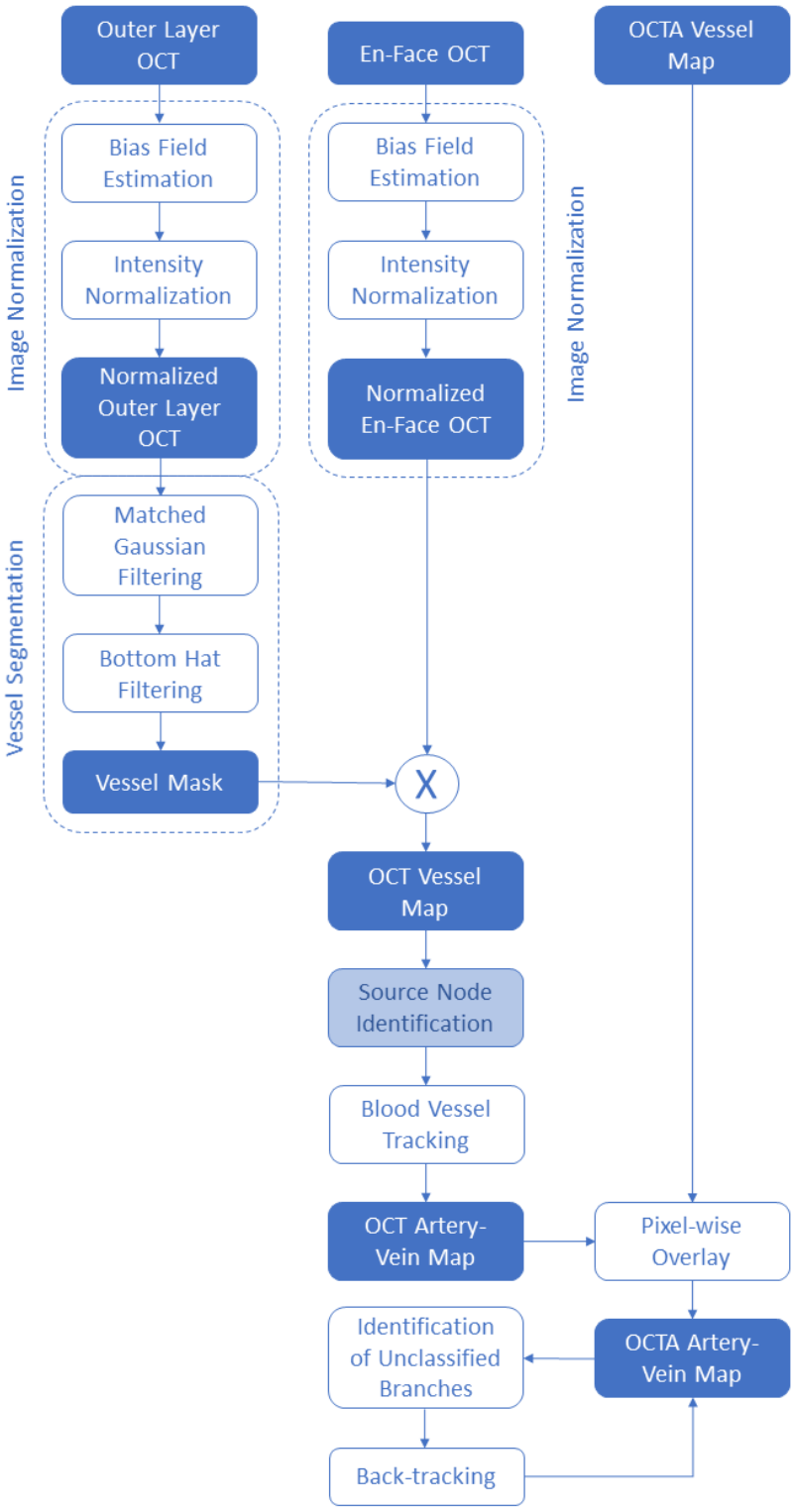


Figure 2.3: Simple flowchart showing the main steps of the Artery-Vein Differentiation algorithm. The blue-colored boxes show inputs and outputs. Adapted from *OCT feature analysis guided artery-vein differentiation in OCTA* [45], March 29 2019, Copyright 2019 by The Optical Society

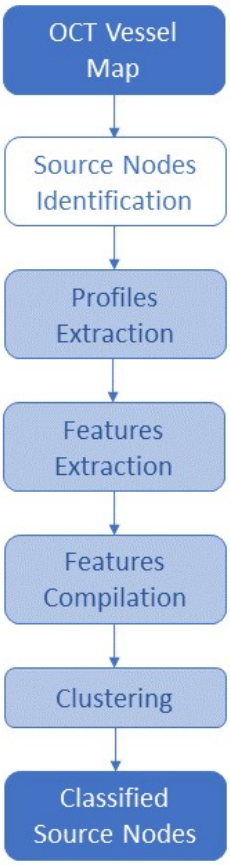


Figure 2.4: Main steps or the Source Node Classification procedure. Adapted from *OCT feature analysis guided artery-vein differentiation in OCTA* [45], March 29 2019, Copyright 2019 by The Optical Society

### 2.3.2 From Outer Layer OCT image to Vessel Mask

Once the Outer Layer OCT image is preprocessed, a mask containing only the pixels belonging to blood vessels must be extracted. Since this layer contains the shadows of the vessels, it is not possible to differentiate them between arteries and veins. However, it has "more contrast with respect to the background, thus making the vessel mask extraction easier" [9]. Figure 2.7 shows the differences between En Face and Outer Layer OCT images. Since the latter contains only the shadows of the vessels, there is no need to correct for the elimination of the macula. The differences in contrast are also clearly visible. It is also worth noting that every pair of images was manually checked for correspondences of blood vessels and shadows. No images were discarded.

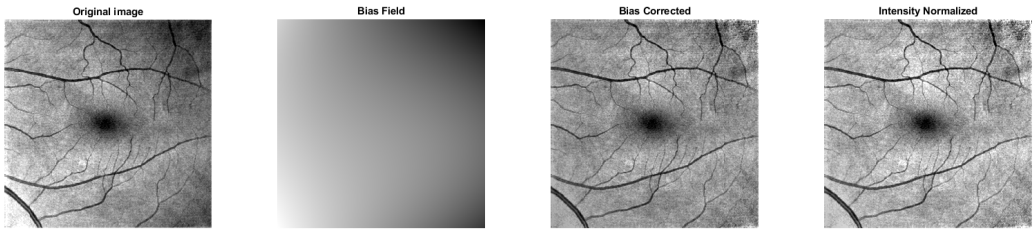


Figure 2.5: Bias Field Correction and Intensity Normalization for an En-Face OCT image. From left to right: the raw image, the estimated Bias Field, the raw image divided by said Bias Field and the image after Intensity Normalization. Adapted from *OCT feature analysis guided artery-vein differentiation in OCTA* [45], March 29 2019, Copyright 2019 by The Optical Society

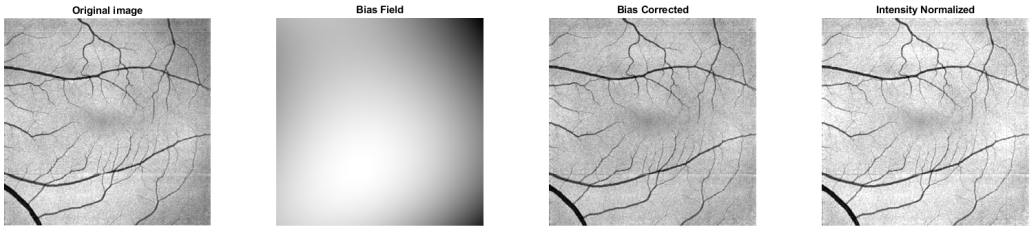


Figure 2.6: Bias Field Correction and Intensity Normalization for an Outer Layer OCT image. From left to right: the raw image, the estimated Bias Field, the raw image divided by said Bias Field and the image after Intensity Normalization. Adapted from *OCT feature analysis guided artery-vein differentiation in OCTA* [45], March 29 2019, Copyright 2019 by The Optical Society

Three steps are needed in order to extract the Vessel Mask:

1. Matched Filtering
2. Bottom-Hat Filtering
3. Binary Thresholding

In order to enhance blood vessels of every diameter and direction, "2D Gaussian kernels of 12 different orientations and 10 different sizes are implemented to match blood vessels" [45]. These 120 2D Gaussian kernels are the ones that were defined by Li et al [47] in 2009. The mean is subtracted from every kernel

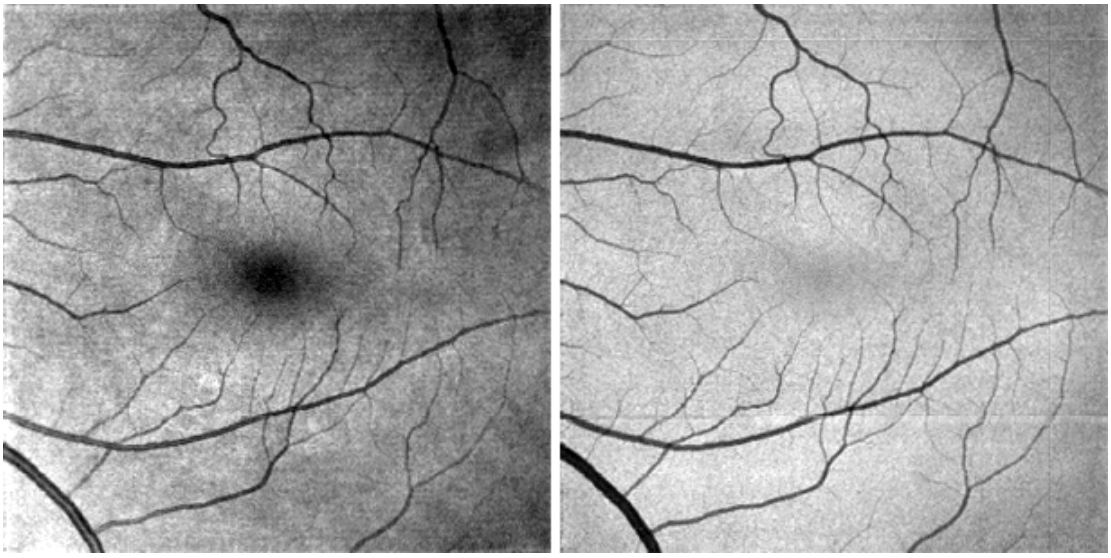

Figure 2.7: En-Face (left) and Outer Layer OCT (right) images of the same eye of the same patient. Adapted from *Differential Artery-Vein Analysis in OCT Angiography of Diabetic Retinopathy* [9], 2021, Copyright 2021 by UIC.

before the convolution with the OCT image. The result of these operations is an image with larger values where vessel-like structures are identified (Figure 2.8 - Top middle). This image is then subtracted from the input OCT image. As can be seen in Figure 2.8 - (Top Right), the resulting image presents an increased contrast between blood vessels and background compared to the input image. Following the improved procedure described in [9], "a selection of four bottom-hat filters with different structural elements and different sizes were applied to the image in parallel and their results were averaged". The result of this step can be seen in Figure 2.8 - (Bottom Left). The last step is to apply a single global threshold to the image in order to binarize it. This threshold is slightly different from image to image, and it was manually selected in order to extract the best quality masks. An example of a generated Vessel Mask can be seen in Figure 2.8 - (Bottom Middle). Every resulting Mask is checked against the corresponding En Face OCT image to assess that the blood vessels of both images coincide (Figure 2.9). Again, no image was discarded during this step. After the Vessel Mask is extracted, it is multiplied with the Intensity Normalized En Face OCT image, as seen following the procedure laid out in Figure 2.3. This output image contains only the intensity values of pixels belonging to blood vessels (Figure 2.8 - Bottom Right), which will be classified in Arteries or Veins in the next steps.

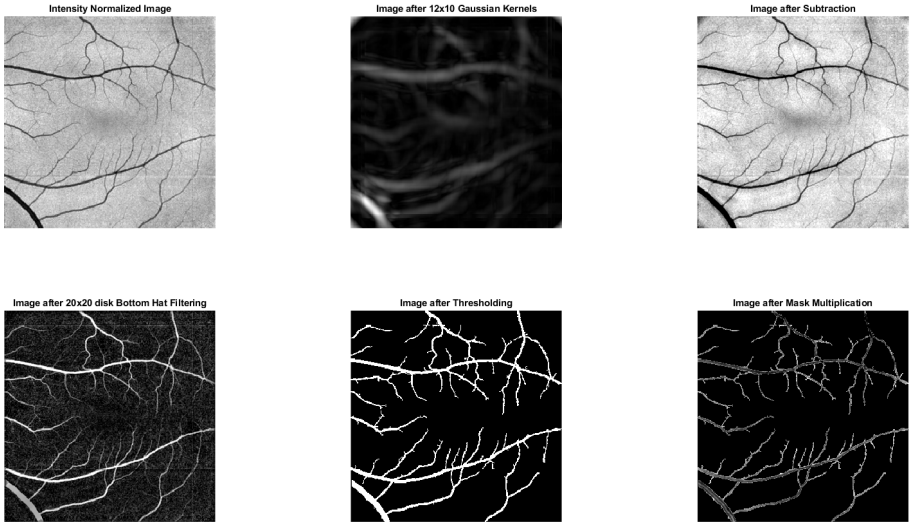


Figure 2.8: Overview of the OCT Vessel Mask generation. Top left: Intensity Normalized Outer Layer OCT image from the previous step. Top middle: mask generated by the Matched Gaussian filtering. Top right: image after subtraction of the mask. Bottom left: image after Bottom-Hat filtering. Bottom middle: image after single threshold binarization. Bottom right: result of the multiplication of the vessel map with the Intensity Normalized En-Face OCT image. Adapted from *Differential Artery-Vein Analysis in OCT Angiography of Diabetic Retinopathy* [9], 2021, Copyright 2021 by UIC.

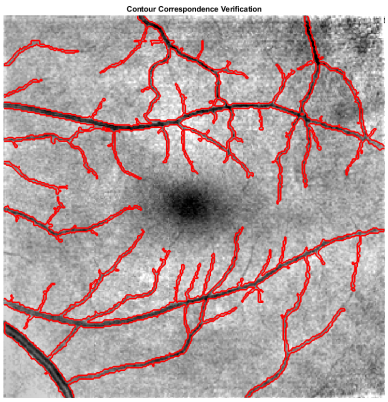


Figure 2.9: Generated graphics used to assess the correspondence between the blood vessels of the Vessel Mask and the ones in the Intensity Normalized En Face OCT image. Adapted from *Differential Artery-Vein Analysis in OCT Angiography of Diabetic Retinopathy* [9], 2021, Copyright 2021 by UIC.

### 2.3.3 Identification of Source Nodes

Once the OCT Intensity Map is generated, the blood vessels are to be classified as either being Arteries or Veins. The procedure was laid out by Alam et al [45] and consists of three steps:

1. Source Node Identification: these nodes are the points in which the vessels cross a set boundary near the image border;

2. Feature Extraction: these features should be capable of classifying every single node.

3. Vessel Tracing: the classification is extended to the whole vessels by tracing them from the start (Source Node) to the end points.

The first of these steps is done by skeletonizing the vessel map and by defining a boundary offset. Skeletonization is a process by which, following multiple erosions of the image, the maximum width of each vessel is exactly one pixel. The boundary offset refers to the pixel gap between the image border and the boundary by which the Source Nodes are identified. The intersections between the skeletonized vessels and the boundary are therefore marked as Source Nodes. This procedure is shown in Figure 2.10 (Left Panel).

### 2.3.4 Extraction of the Profiles

The concept of 'Profiles' was defined by Vàsquez et al [48]. Small windows centered on each Source Node allow to extract vessel and skeleton segments. Starting from the skeletons, a set of profiles is created [45]. Two profiles must have a distance of two pixels between them along the skeleton segment. The number of profiles must be at least 5 and can not be more than 20. "In case of a segment smaller than 5 pixels long, profiles are taken from all of the pixels". The first profile is always located on the midpoint of the extracted segment. The others are iteratively constructed by moving by two pixels in each direction. Figure 2.10 (Middle Panel) shows this procedure.

This operation identified multiple profiles for each Source Node segment. A 'Profile Set' is created to store the profiles grouped by Source Node. For example, the OCT image used as reference in these Figures has 14 identified Source Nodes. Therefore, 14 profile sets will be created, each one with a different number of profiles.

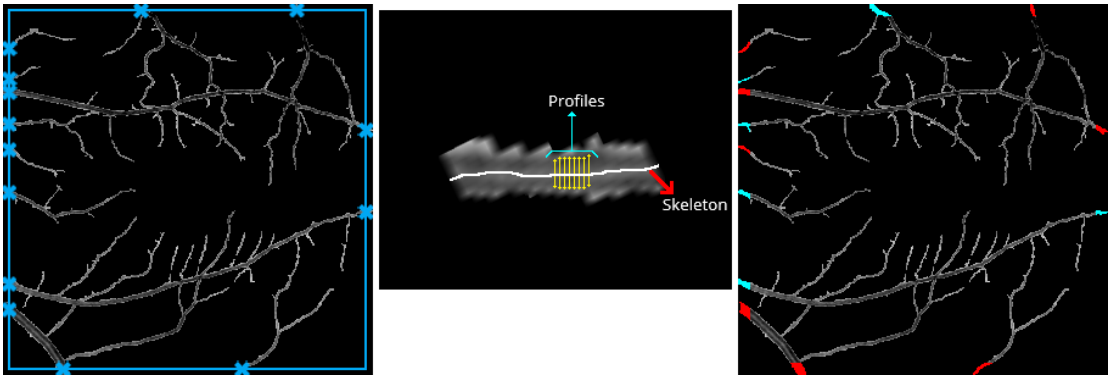


Figure 2.10: Overview of the Source Node Classification procedure. Left: the Source Nodes (blue crosses) are located. Middle: some Profiles (in yellow) are created along a Source Node Segment. Right: Source Nodes classified as arteries (in red) or veins (in teal). Adapted from *OCT feature analysis guided artery-vein differentiation in OCTA* [45], March 29 2019, Copyright 2019 by The Optical Society

### 2.3.5 Source Node Classification

For every profile in every profile set, four features are extracted. These features are introduced and explained by Alam et al [45]:

- Ratio of Vessel Width to Central Reflex (RWCR);
- Average of Maximum Profile Brightness (AMPB);
- Average of Median Profile Intensity (AMPI);
- Optical Density of Vessel Boundary Intensity compared to Background Intensity (ODVB).

The averaged and normalized distributions of these four features in Arteries and Veins is shown in Figure 2.11. It can be seen that RWCR and ODVB have the better discriminating capability.

Once we have the full set of the features, the classification process can begin. Arteries and Veins are identified via K-means clustering, where there are two possible clusters. The results are reliable and efficient and does not require much computation power [45]. The cluster centers are initialized to be the two input points farthest away from each other. Euclidean distancing was used to measure the distance between points. Three steps were introduced to maximize the accuracy of the algorithm:

1. The K-means classification is applied to every segment of the Source Nodes;

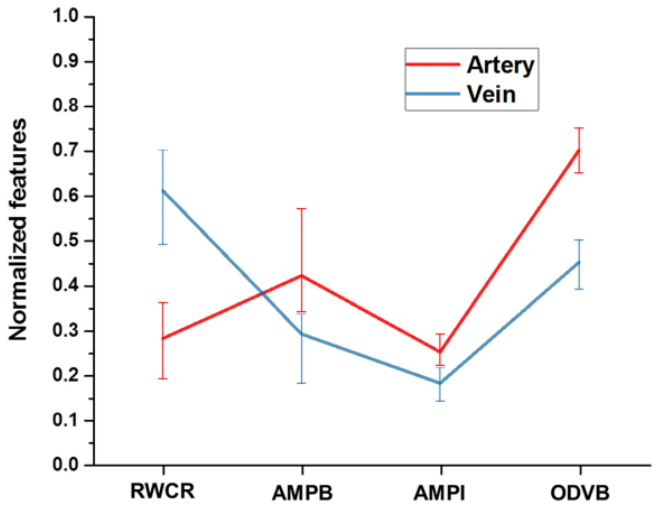


Figure 2.11: Normalized feature distribution in artery and vein vessels. RWCR: ratio of width to central reflex; AMPB: average of maximum profile brightness; AMPI: average of median profile intensity; ODVB: optical density of vessel boundary. Reprinted from *OCT feature analysis guided artery-vein differentiation in OCTA* [45], March 29 2019, Copyright 2019 by The Optical Society.

2. The image is subdivided into four quadrant. The k-means predictions are separately calculated for each quadrant. This is done to minimize the effect of the inhomogeneous intensity distributions of the quadrants on the final estimation;

3. The quadrants are rotated by 45°. The classification is re-performed on every quadrant each time they rotate. In order to reach 360°, a total of eight rotations have to be performed. Thus, eight predictions will be present for each Source Node. This is illustrated in Figure 2.12. Rotations of 45° make the quadrants overlap. This step complements the second one.

The final classification for each node will be chosen based on the eight predictions. A majority vote is enough to eliminate errors due to outlier predictions.

### 2.3.6 Vessel Tracking

Once all Source Nodes are classified into arteries or veins, the rest of the vessel structures must be classified as well. Alam et al. developed a blood vessel tracking algorithm for this purpose [10]. Figure 2.13 contains a pipeline of such procedure.

The starting point is a Source Node. A grid (initially 3 by 3 pixels) is used to locate the pixels belonging to the vessel. When a pixel is not found, the grid is enlarged. This process is repeated until an intersection is found. Here, the algorithm has to identify the main branch of the vessel. This decision is based on

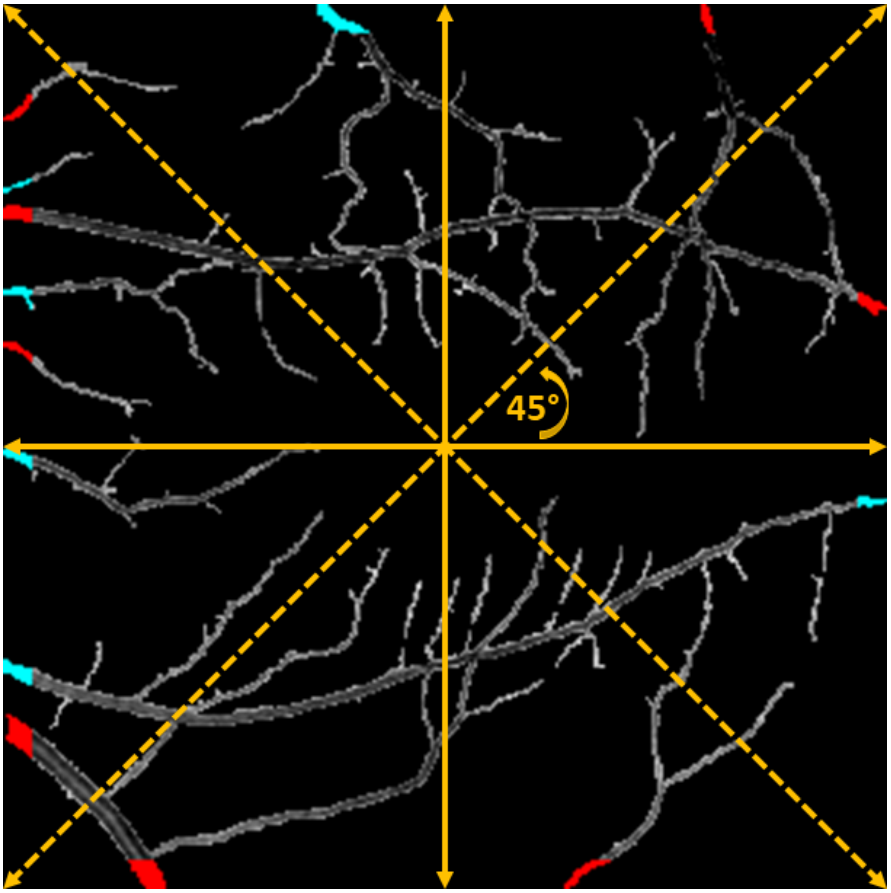


Figure 2.12: Illustration of the eight rotations of the quadrants. The center of rotations is the fovea (at the center of the OCT image). Adapted from *OCT feature analysis guided artery-vein differentiation in OCTA* [45], March 29 2019, Copyright 2019 by The Optical Society.

curvature and angle information. Panel C of Figure 2.14 shows a vessel bifurcation, upon which four points are located:

- P0, which identifies the branch that leads to the Source Node;
- P1, which identifies the bifurcation point;
- P2 and P3, which identify the two paths that that vessel takes once it splits.

These four points are used to identify two curves: P0-P1-P2 and P0-P1-P3. For each curve,a curvature metric is defined by Alam et al [10]. "The path with smaller curvature is therefore considered the main branch and it will be used by the algorithm to advance forward" [9]. Moreover, the path with the greatest angle (X and Y in Figure 2.14 - C) is also taken into account. After having located the main path, the algorithm marks the unused branch and follows the main one.

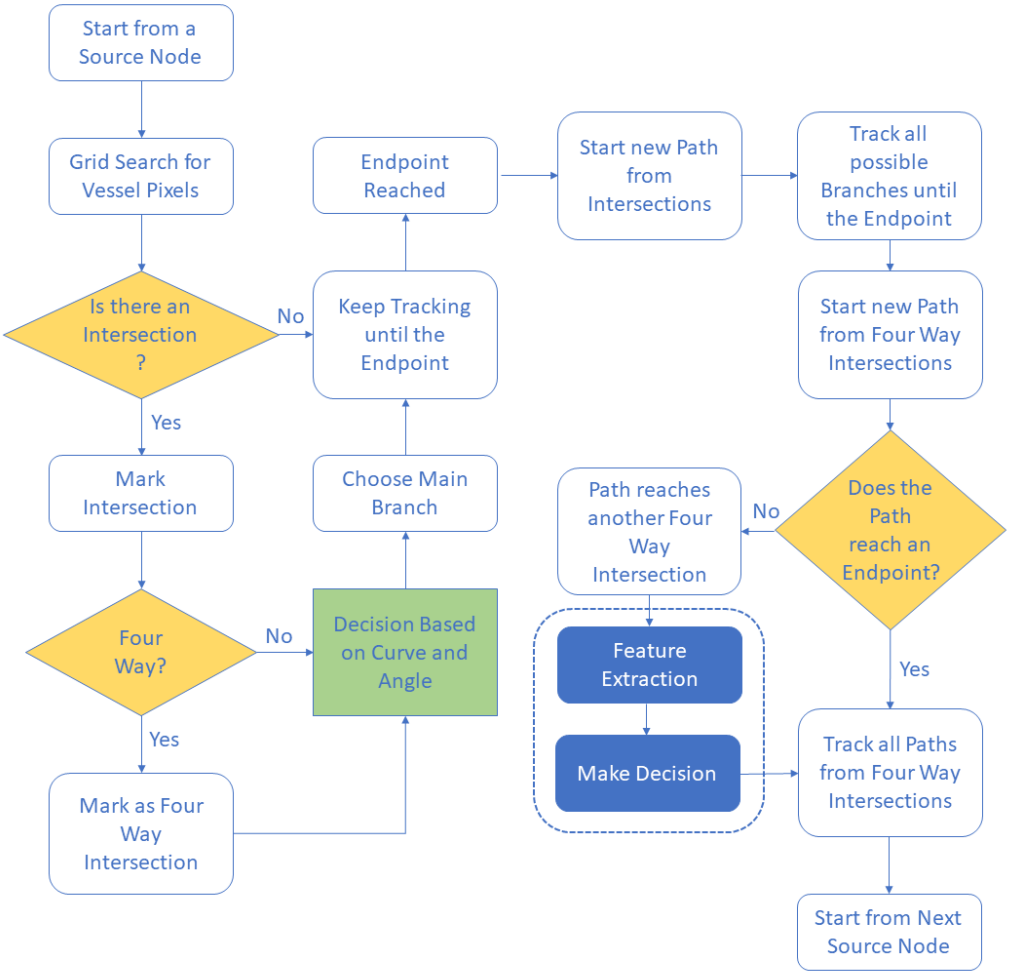


Figure 2.13: Flowchart of the Blood Vessel Tracking procedure. Adapted from *Combining ODR and Blood Vessel Tracking for Artery- Vein Classification and Analysis in Color Fundus Images* [10], April 2018, Copyright 2018 by ARVO Journals.

Whenever a four-way intersection is reached, the decision is made once all the normal bifurcations in the image have been resolved. When the endpoint of the main branch is reached, the algorithm starts from one of the marked secondary paths. When all of the bifurcations of a vessel are classified, the whole process restarts from a new Source Node. When the four-way intersections are the only ones to remain unclassified, the final phase of the procedure begins. Every four-way intersection belongs to one of two cases: either it is a crossing point of two different vessels or it is a case of a single vessel with multiple branching. In order

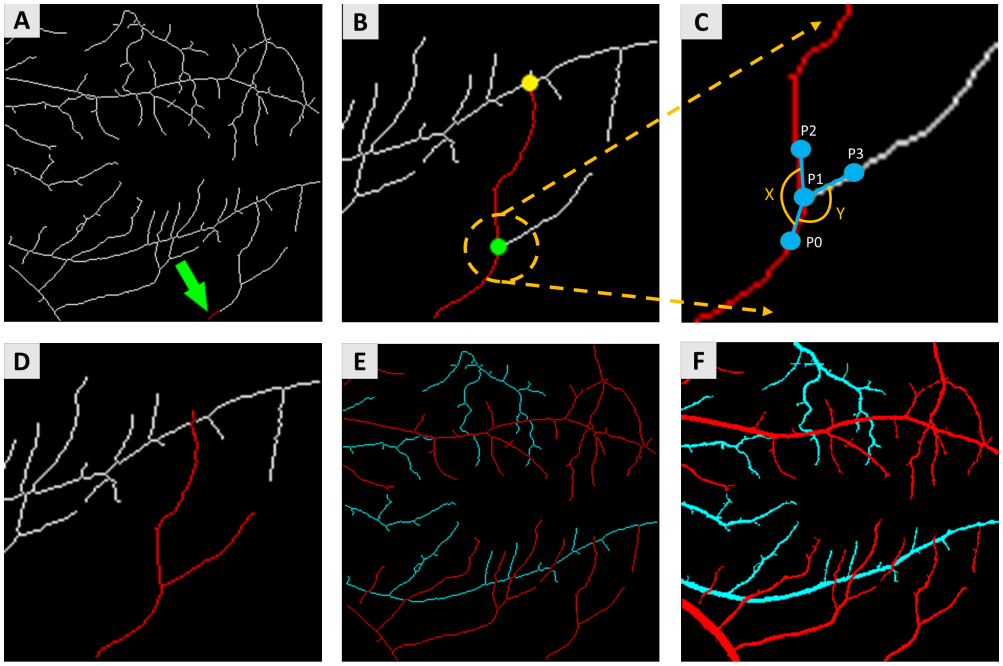


Figure 2.14: Core steps of the Vessel Tracking algorithm. A: the algorithm starts from a Source Node. B: the main branch of the vessel is tracked; the green dots represent the encountered branch nodes. One four-way intersection is marked with a yellow dot. C: enlarged window showing the process of choosing the forward path in the vessel map. D: the whole vessel is identified. E: these steps are repeated until the Skeleton Map is completely classified in arteries (red) and vein (teal). F: fully classified OCT Vessel Map. Adapted from *Combining ODR and Blood Vessel Tracking for Artery- Vein Classification and Analysis in Color Fundus Images* [10], April 2018, Copyright 2018 by ARVO Journals.

to ascertain their type, the four branches are back-tracked until they reach an endpoint or another intersection. If an endpoint is reached, then the branch is classified in the same way as the main branch. If an intersection is reached, every branch is classified by the algorithm by comparing textural parameters between the branches and between all classified vessels. When this process is concluded, the Skeleton Map is fully classified (Figure 2.14 - E).

### 2.3.7 Generating the Classified OCTA Vessel Map

The classified Skeleton Map is used in combination with the binary OCTA Vessel Map to generate the final Classified Vessel Map. "The en face OCT and OCTA images are generated from 3D projection of OCT B-scans and B-Scan speckle variance images, respectively. This means the structural coordinates of both images are same" [45]. The classification can thus be directly transferred from OCT to OCTA, without the need of complex methods of overlaying. This simple pro-

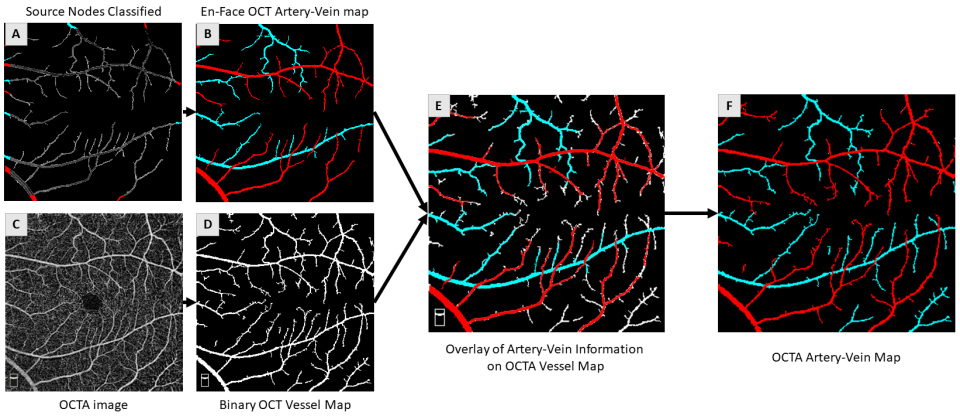


Figure 2.15: Artery-Vein classification in OCTA. A: classified source nodes in OCT vessel map. B: OCT artery-vein map. C: original OCTA image. D: OCTA binary vessel map. E: OCT artery-vein map overlaid onto the OCTA binary vessel map. F: final OCTA artery-vein map. Adapted from *OCT feature analysis guided artery-vein differentiation in OCTA* [45], March 29 2019, Copyright 2019 by The Optical Society.

cess covers the bigger blood vessels. However, the smaller vessels that appear in OCTA images but are absent in OCT images have to be classified in a different way. They have to be traced in a similar way to the vessel tracking occurred in Section 2.4.6. "It starts in the skeleton map: from the endpoint of an unclassified vessel and back-tracks until it reaches a classified vessel, and then begins again from another endpoint. Four-ways intersections are treated in the same way as before" [9]. When this step is completed, the Classified OCTA Vessel Map is completed. Figure 2.15 shows the workflow of the OCTA Artery-Vein Map generation.

## 2.4 Generating Arteries and Veins Maps

The Classified OCTA Maps must be further processed in order to measure the features. The last two steps are:

- Separating Arteries from Veins;
- Bridging the gaps in the Vein Maps.

### 2.4.1 Separating Arteries from Veins

Separating Arteries from Veins is very simple. The two types of vessels are saved in the Classified OCTA Map with two different colors: red for the Arteries and teal for the Veins. A short MATLAB procedure can extract the two different

colors and separate them in two images: one with only the red pixels (Arteries) and one with only the teal pixels (Veins). Figure 2.16 shows the result of this step.

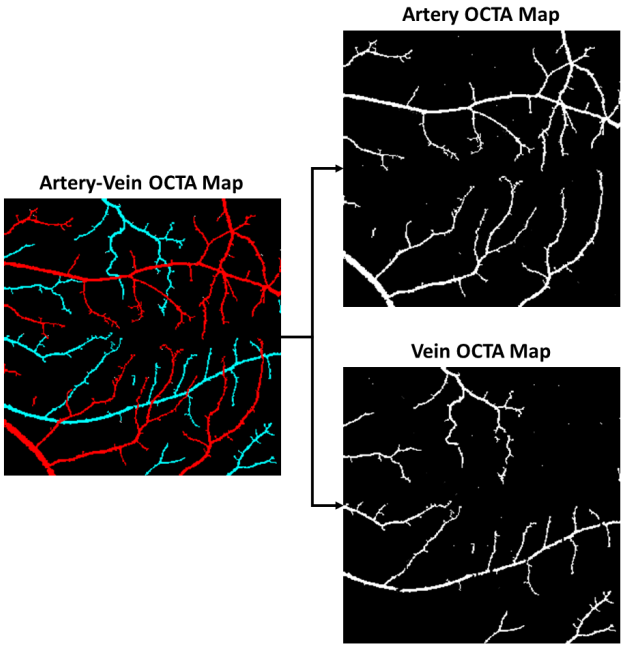


Figure 2.16: Input and Outputs of the Artery-Vein Separation procedure. Adapted from *Differential Artery-Vein Analysis in OCT Angiography of Diabetic Retinopathy* [9], 2021, Copyright 2021 by UIC.

### 2.4.2 Bridging the gaps in the Vein Maps

As can be seen in Figure 2.16, the Vein Map has many gaps along its vessels. This is because there are many instances of four-way crossings between vessels of different types. Usually, Arteries are the ones that cross over Veins. Thus, by arbitrary convention, the algorithm favors the integrity of Arteries, which are always made to cross over Veins in the Classified OCTA Map. This leaves the Vein Map with gaps. A custom MATLAB procedure was conceived in order to bridge those gaps, taking advantage of morphological transformations of the binary Vein Map. This Bridged Vein Map (Figure 2.17 - Right) is used in this study. Note that not all the gaps are closed: the largest ones are still unbridged. However, the vast majority of the gaps are bridged without compromising the original structure of the vessels, which is the most important aspect to consider.

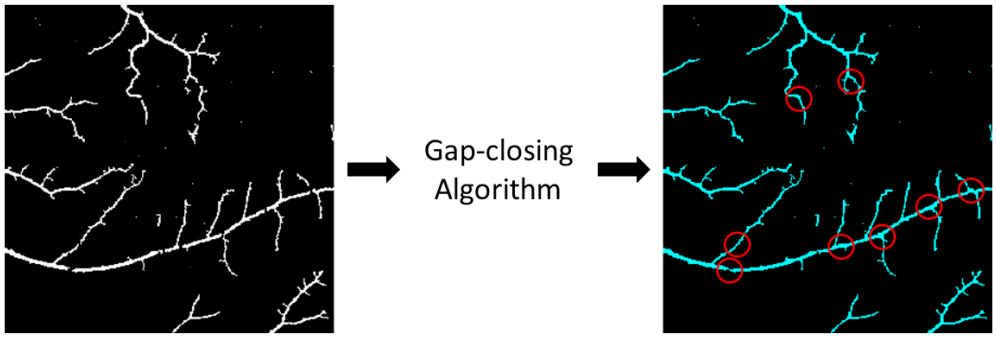


Figure 2.17: Transition from unbridged Vein Map (Left) to Bridged Vein Map (Right). The red circles locate the bridged gaps.

## 2.5 Features

### 2.5.1 Description of the Six Features

In this study, six parameters will be measured by an automatic custom MATLAB procedure. These features are:

- Vessel Perimeter Index (VPI): it measures the share of pixels in vessel perimeters compared to the total area of the image. It is defined by Chu et al. [35] as:

$$VPI = \frac{\Sigma_{i=1,j=1}^{n} P_{(i,j)}}{\Sigma_{i=1,j=1}^{n} T_{(i,j)}} \tag{2.1}$$

  where $P_{(i,j)}$ represents all the white pixels along the vessels' perimeters, and $T_{(i,j)}$ represents the total area of pixels in the image;

- Vessel Diameter Index (VDI): it represent an approximation of the mean diameter of the vessels in the image. It is defined by Chu et al. [35] as:

$$VDI = \frac{\Sigma_{i=1,j=1}^{n} A_{(i,j)}}{\Sigma_{i=1,j=1}^{n} S_{(i,j)}} \tag{2.2}$$

  where $A_{(i,j)}$ represents all the white pixels in the vessels' areas, and $S_{(i,j)}$ all the white pixels in the vessels' skeletons;

- Vessel Skeleton Density (VSD): it measures the share of pixels in vessel skeletons compared to the total area of the image. It is defined by Chu et al. [35] as:

$$VSD = \frac{\Sigma_{i=1,j=1}^{n} S_{(i,j)}}{\Sigma_{i=1,j=1}^{n} T_{(i,j)}} \tag{2.3}$$

  where $S_{(i,j)}$ represents all the white pixels in the vessels' skeleton, and $T_{(i,j)}$ represents the total area of pixels in the image;

- Vessel Area Density (VAD): it measures the share of pixels in vessel areas compared to the total area of the image. It is defined by Chu et al. [35] as:

$$VAD = \frac{\Sigma_{i=1,j=1}^{n} A_{(i,j)}}{\Sigma_{i=1,j=1}^{n} T_{(i,j)}} \tag{2.4}$$

  where $A_{(i,j)}$ represents all the white pixels in the vessels' areas, and $T_{(i,j)}$ represents the total area of pixels in the image;

- Vessel Complexity Index (VCI): it is a parameter that is used to represent visual complexity of the pattern of the vessels. It is defined by Chu et al. [35] as:

$$VCI = \frac{(\Sigma_{i=1,j=1}^{n} P_{(i,j)})^2}{4\pi\Sigma_{i=1,j=1}^{n} A_{(i,j)}} \tag{2.5}$$

  where $P_{(i,j)}$ represents all the white pixels along the vessels' perimeters, and $A_{(i,j)}$ represents all the white pixels in the vessels' areas;

- Fractal Dimension (FD): like VCI, it is used to represent visual complexity of the vasculature. It is also linked to vessel tortuosity. This parameter is calculated using the Box-Counting method on the skeletons of the vessels [40].

### 2.5.2 Measurement of the Features

This procedure is simple and straight-forward. First, the images are cleaned of any spurious pixels. When the images are cleaned (Figure 2.18 - A), the Perimeter Map (Figure 2.18 - B) and the Skeleton Map (Figure 2.18 - C) are generated. Then, $T_{(i,j)}$, $A_{(i,j)}$, $S_{(i,j)}$ and $P_{(i,j)}$ are counted. After this, five of the six features (VPI, VDI, VSD, VAD and VCI) are calculated. The Fractal Dimension is computed via a separate MATLAB procedure. The measured values of the features are saved separately for each cohort. The measures for Arteries and Veins are done independently.

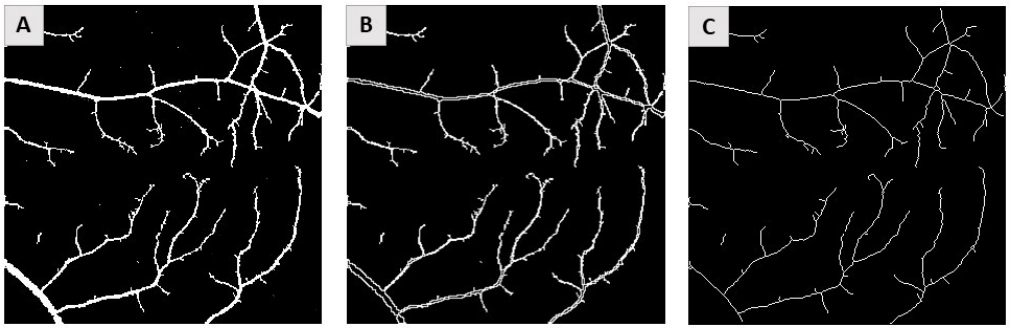


Figure 2.18: Images used for the Feature Computation: Vessel Map (Left), Perimeter Map (Center) and Skeleton Map (Right).

## 2.6 Feature Sets

The six features mentioned above are measured two times (Arteries and Veins). Two other feature sets are derived from these two measurements. In order, the four feature sets that will be analyzed in this study are:

- ARTERY: set composed of features extracted from Artery Maps;
- VEIN: set composed of features extracted from Vein Maps;
- A/V Ratio: set composed of the ratios between artery and vein features:

$$A/VFeature = \frac{Feature_A}{Feature_V} \tag{2.6}$$

- AVERAGE: set composed of the arithmetic averages between artery and vein features:

$$AverageFeature = \frac{Feature_A + Feature_V}{2} \tag{2.7}$$

## 2.7 Statistical Analysis Protocol

In this section, the protocol of the Statistical Analysis conducted in this study is described. Since the Gaussianity of the distributions is not guaranteed, Kruskal-Wallis and Mann-Whitney tests were used instead of ANOVAs and t-tests. First, the Mild, Moderate and Severe cohorts are put together to form a unique NPDR cohort that is comprised of only patients with the illness. A Kruskal-Wallis Test is performed on the three main cohorts (Control, NoDR and NPDR). This is done in

order to see whether the three cohorts are statistically different from one another. For the features that showed statistical significance (p <0.05), a series of three Mann-Whitney tests were performed:

- Control vs NoDR
- Control vs NPDR
- NoDR vs NPDR

The p-values of these tests were corrected using the Bonferroni Correction. These tests were done in order to see in detail which distributions were separable. Then, another Kruskal-Wallis Test is performed on the three NPDR cohorts (Mild, Moderate and Severe NPDR). The purpose of this test is to see if the three stages of NPDR have feature distributions that can be separated from each other. Again, for the features that showed statistical significance (p ¡ 0.05), a series of three Mann-Whitney tests were performed:

- Mild NPDR vs Moderate NPDR
- Mild NPDR vs Severe NPDR
- Moderate NPDR vs Severe NPDR

Again, the p-values of these tests were corrected using the Bonferroni Correction. These tests were done in order to see in detail which distributions were separable.

# Chapter 3

# Results

Before showing the results, it is worth noting that the patients' demographics are the same as the study by Castelnuovo [9] and the work by Le et al [25]. The distributions of age, sex and hypertension were not statistically different between the NPDR cohorts and the Control patients.

## 3.1 First Kruskal-Wallis Tests

These tests were performed in order to see whether the Control, NoDR and NPDR cohorts have statistically different distributions. A summary of the distribution of the features for the three cohorts and their p-values are shown in the next sections.

### 3.1.1 Artery Features

The following table shows the median values values and the 25th and 75th percentiles of the distributions of the cohorts, alongside the Kruskal-Wallis p-value, for the features measured on the Artery Vessel Maps:

| Features | Control | NoDR | NPDR | p-values |
|---|---|---|---|---|
| **VPI** | 0.055 (0.043-0.064) | 0.053 (0.050-0.059) | 0.063 (0.048-0.073) | **0.0242** |
| **VDI** | 2.549 (2.445-2.661) | 2.744 (2.603-2.827) | 2.574 (2.444-2.754) | **0.0068** |
| **VSD** | 0.024 (0.019-0.028) | 0.023 (0.020-0.025) | 0.026 (0.020-0.031) | 0.055 |
| **VAD** | 0.063 (0.049-0.071) | 0.061 (0.057-0.067) | 0.067 (0.054-0.081) | 0.2029 |
| **VCI** | 359.4 (273.9-472.9) | 565.4 (426.6-635.6) | 432.2 (346.2-521.4) | **0.0006** |
| **FD** | 1.384 (1.337-1.419) | 1.392 (1.367-1.417) | 1.406 (1.339-1.448) | 0.2393 |

Table 3.1: Distributions and p-values of the Artery Features.

Based on the p-values, it can be asserted that VPI, VDI and VCI are able to differentiate at least one cohort from the other two, with a greater emphasis on the latter.

### 3.1.2 Vein Features

The following table shows the median values values and the 25th and 75th percentiles of the distributions of the cohorts, alongside the Kruskal-Wallis p-value, for the features measured on the Vein Vessel Maps:

| Features | Control | NoDR | NPDR | p-values |
|---|---|---|---|---|
| **VPI** | 0.047 (0.043-0.059) | 0.048 (0.042-0.054) | 0.051 (0.040-0.060) | 0.625 |
| **VDI** | 2.689 (2.615-2.780) | 2.945 (2.865-3.116) | 2.769 (2.601-2.963) | **0.0002** |
| **VSD** | 0.021 (0.018-0.025) | 0.020 (0.017-0.022) | 0.021 (0.016-0.025) | 0.4169 |
| **VAD** | 0.058 (0.050-0.066) | 0.059 (0.049-0.066) | 0.059 (0.044-0.071) | 0.9999 |
| **VCI** | 309.0 (271.8-413.0) | 468.4 (377.2-550.5) | 352.5 (274.0-427.9) | **0.0008** |
| **FD** | 1.353 (1.326-1.393) | 1.362 (1.323-1.388) | 1.363 (1.309-1.403) | 0.9851 |

Table 3.2: Distributions and p-values of the Vein Features.

Based on the p-values, it can be asserted that VDI and VCI are able to differentiate at least one cohort from the other two, with a greater emphasis on the former.

### 3.1.3 A/V Differential Features

The following table shows the median values values and the 25th and 75th percentiles of the distributions of the cohorts, alongside the Kruskal-Wallis p-value, for the ratios of the features measured on the Artery Vessel Maps and the ones measured on the Vein Vessel Maps:

| Features | Control | NoDR | NPDR | p-values |
|---|---|---|---|---|
| **VPI** | 1.089 (0.943-1.209) | 1.077 (0.957-1.241) | 1.221 (1.090-1.382) | **0.0021** |
| **VDI** | 0.958 (0.921-0.993) | 0.932 (0.892-0.962) | 0.936 (0.910-0.966) | 0.0993 |
| **VSD** | 1.107 (0.982-1.225) | 1.114 (0.965-1.274) | 1.235 (1.100-1.407) | **0.0038** |
| **VAD** | 1.063 (0.946-1.177) | 1.008 (0.894-1.197) | 1.178 (1.033-1.309) | **0.0087** |
| **VCI** | 1.113 (0.983-1.264) | 1.144 (1.020-1.321) | 1.280 (1.125-1.438) | **0.0019** |
| **FD** | 1.017 (0.996-1.034) | 1.021 (0.996-1.035) | 1.032 (1.014-1.056) | **0.0115** |

Table 3.3: Distributions and p-values of the A/V Differential Features.

Based on the p-values, it can be asserted that, apart from VDI, every feature is able to differentiate at least one cohort from the other two. These are very encouraging results, possibly suggesting that the A/V Ratios of the features carry a high significance and can be used to aid the diagnosis of Diabetic Retinopathy.

### 3.1.4 Average Features

The following table shows the median values values and the 25th and 75th percentiles of the distributions of the cohorts, alongside the Kruskal-Wallis p-value, for the averages of the features measured on the Artery Vessel Maps and the Vein Vessel Maps:

| Features | Control | NoDR | NPDR | p-values |
|---|---|---|---|---|
| **VPI** | 0.049 (0.044-0.064) | 0.051 (0.045-0.057) | 0.058 (0.045-0.066) | 0.1275 |
| **VDI** | 2.603 (2.567-2.692) | 2.861 (2.706-3.015) | 2.656 (2.521-2.875) | **0.0005** |
| **VSD** | 0.021 (0.019-0.027) | 0.021 (0.019-0.024) | 0.024 (0.019-0.028) | 0.167 |
| **VAD** | 0.057 (0.052-0.069) | 0.063 (0.052-0.066) | 0.064 (0.051-0.075) | 0.5857 |
| **VCI** | 320.5 (281.6-436.9) | 498.4 (391.3-579.9) | 395.4 (320.3-460.5) | **0.0006** |
| **FD** | 1.357 (1.339-1.408) | 1.377 (1.352-1.402) | 1.389 (1.331-1.420) | 0.6538 |

Table 3.4: Distributions and p-values of the Average Features.

Based on the p-values, it can be asserted that, similarly with the Vein Features, VDI and VCI are able to differentiate at least one cohort from the other two. It is worth noting that VCI's p-values are all below the significance threshold.

## 3.2 First Mann-Whitney Tests

After the Kruskal-Wallis tests, a number of promising features can be identified. Therefore, three Mann-Whitney statistical tests are performed in order to see which cohorts could be separated from each other. The three tests are:

- Control vs NoDR
- Control vs NPDR
- NoDR vs NPDR

The first test is done to see the differences in the features' distributions due to the presence of Diabetes Mellitus only. The second is done to see the differences in the features' distributions due to both Diabetes and Diabetic Retinopathy. The final test is done to see the differences in the features' distributions due to the presence of NPDR only, since both cohorts' patients have Diabetes Mellitus.

### 3.2.1 Bonferroni Correction

As the number of statistical hypotheses which are tested increases, the probability of observing rare events also increases [49]. This is the basis of the Bonferroni Correction. Since three hypotheses are tested for each feature (the three tests mentioned above), the probability of having False Positives (type I errors) is increased by a factor of three. In order to account this increase, the Bonferroni Correction states that the threshold of p-value significance should by divided by the same factor. Thus, the significance threshold for these Mann-Whitney tests has to be 0.0166. This technique is very conservative, and suffers from an increase in False Negatives (type II errors). Therefore, p-values that do not pass the new significance threshold but are still lower than the original threshold will be marked with the * symbol, while the p-values that pass the new significance threshold will be shown in bold.

### 3.2.2 First Mann-Whitney Test: Control vs NoDR

The Mann-Whitney p-values for the Control vs NoDR cohort test are shown in the next table:

| p-values | VPI | VDI | VSD | VAD | VCI | FD |
|---|---|---|---|---|---|---|
| **Artery** | 0.6241 | **0.005** | 0.3735 | 0.8337 | **0.0001** | 0.6818 |
| **Vein** | 0.4593 | **0.0001** | 0.1770 | 0.9442 | **0.0002** | 0.9124 |
| **A/V Ratio** | 0.9681 | 0.0561 | 0.9045 | 0.6745 | 0.4413 | 0.9124 |
| **Average** | 0.6745 | **0.0002** | 0.3222 | 0.9442 | **0.0001** | 0.7566 |

Table 3.5: p-values of the Control vs NoDR Mann-Whitney test.

It can be seen that only two features, namely VDI and VCI, are able to differentiate patients with Diabetes Mellitus from control patients.

### 3.2.3 Second Mann-Whitney Test: Control vs NPDR

The Mann-Whitney p-values for the Control vs NPDR cohort test are shown in the next table:

| p-values | VPI | VDI | VSD | VAD | VCI | FD |
|---|---|---|---|---|---|---|
| **Artery** | 0.0949 | 0.8337 | 0.2380 | 0.2150 | 0.0293* | 0.1645 |
| **Vein** | 0.7339 | 0.3222 | 0.6672 | 0.9920 | 0.3371 | 0.8808 |
| **A/V Ratio** | **0.0025** | 0.1010 | **0.0032** | **0.0160** | **0.0014** | **0.0078** |
| **Average** | 0.3222 | 0.6892 | 0.6101 | 0.5419 | 0.1052 | 0.4902 |

Table 3.6: p-values of the Control vs NPDR Mann-Whitney test.

It can be seen that only the A/V Ratio features, with the exception of VDI, are able to differentiate between Control and NPDR patients. This suggests that the relative changes of these features in Arteries and Veins have the potential to help to better understand and diagnose Diabetic Retinopathy in its Non-Proliferative stage.

### 3.2.4 Third Mann-Whitney Test: NoDR vs NPDR

The Mann-Whitney p-values for the NoDR vs NPDR cohort test are shown in the next table:

| p-values | VPI | VDI | VSD | VAD | VCI | FD |
|---|---|---|---|---|---|---|
| **Artery** | **0.0111** | **0.0032** | 0.0188* | 0.1188 | **0.0124** | 0.2150 |
| **Vein** | 0.3421 | **0.0003** | 0.2937 | 0.9761 | **0.0016** | 0.9681 |
| **A/V Ratio** | **0.0143** | 0.2757 | 0.0257* | **0.0155** | 0.0293* | 0.0488* |
| **Average** | 0.0394* | **0.0005** | 0.05* | 0.3173 | **0.0047** | 0.4473 |

Table 3.7: p-values of the NoDR vs NPDR Mann-Whitney test.

It can be seen that, in contrast to the previous tests, there are many p-values marked with the * symbol, making the interpretation of the table tricky. Also, there are some features that have a significant p-value only with specific measuring modalities. For example, VPI's p-values are below the threshold only if measured on Arteries and if the A/V Ratio is taken. VPI measures on Veins only do not seem to be informative.

## 3.3 Box and Whiskers Plots

To better visualize the differences and similarities between the distributions of the cohorts, one box and whisker plot per feature is shown in this section. A distribution is marked if it is significantly different from the other two or only one of the other distributions. For simplicity's sake, only p-values that passed the Bonferroni Correction were used.

### 3.3.1 VPI Box and Whisker Plot

The next graph shows the distributions of the Vessel Perimeter Index (VPI) across the four feature sets:

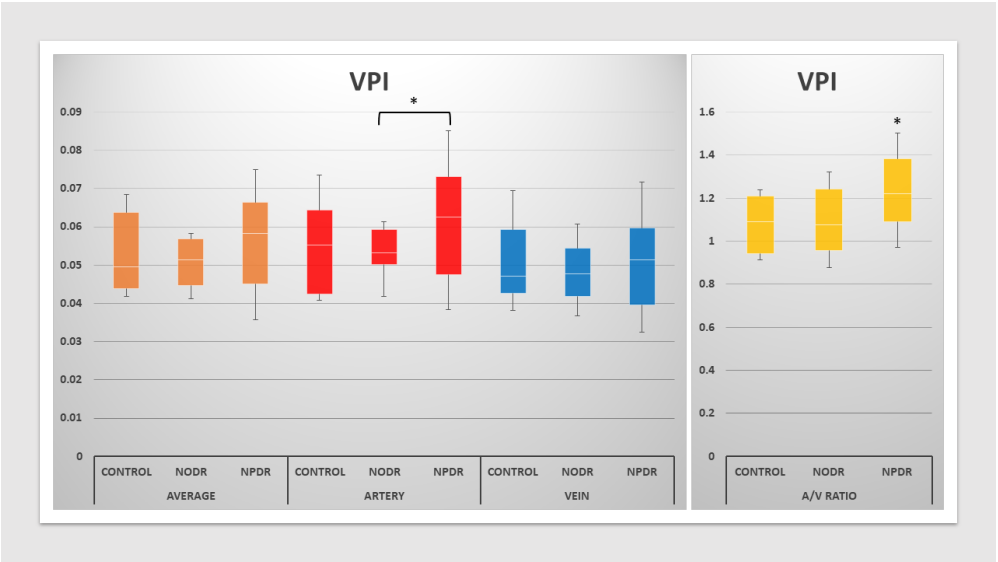


Figure 3.1: VPI Box and Whisker Plot

As can be seen, the Artery NoDR and NPDR distributions can be differentiated: the former has a very narrow shape compared to the latter. More importantly, the A/V Ratio NPDR distribution is separable from the cohorts without Diabetic Retinopathy.

### 3.3.2 VDI Box and Whisker Plot

The next graph shows the distributions of the Vessel Diameter Index (VDI) across the four feature sets:

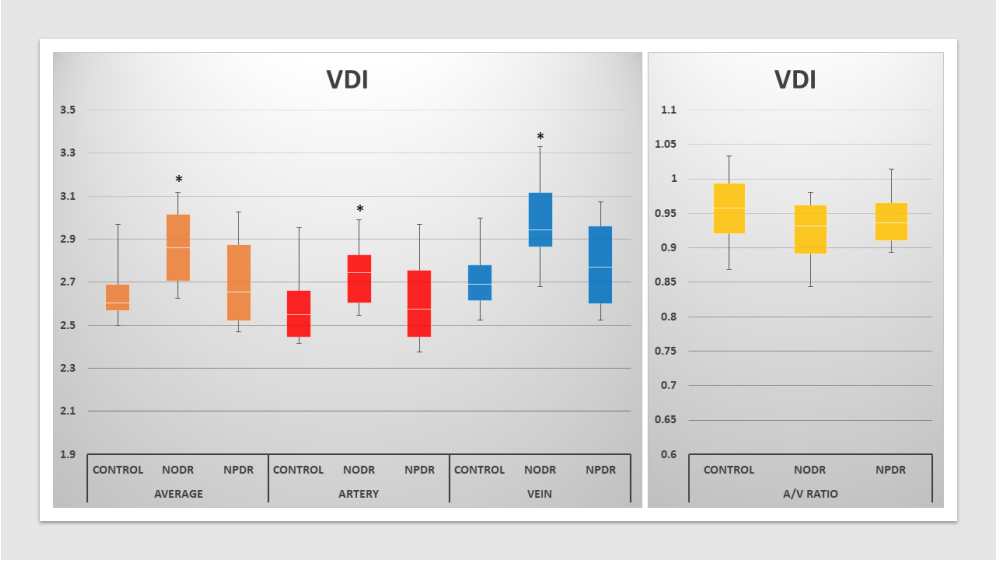


Figure 3.2: VDI Box and Whisker Plot

As can be seen, in the Artery, Vein and Average measurements, the NoDR distributions are significantly higher than the other two distributions, especially the Control ones.

### 3.3.3 VSD Box and Whisker Plot

The next graph shows the distributions of the Vessel Skeleton Density (VSD) across the four feature sets:

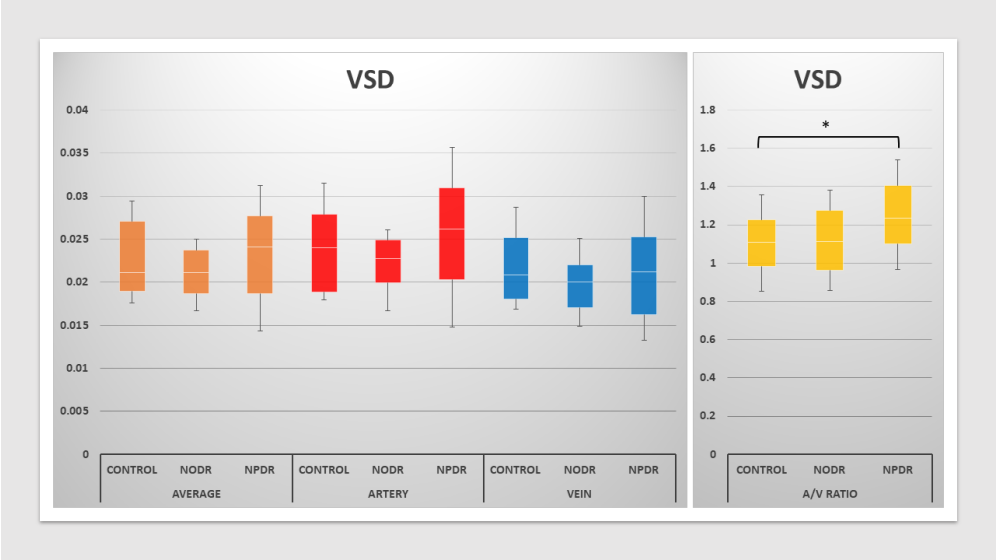


Figure 3.3: VSD Box and Whisker Plot

As can be seen, this feature does not seem to be that useful. The only differentiable distributions are the A/V Ratio Control and NPDR ones, which follow the trend seen in VPI (and that will be seen in other features): a sudden increase in A/V Ratio values for the patients with Diabetic Retinopathy.

### 3.3.4 VAD Box and Whisker Plot

The next graph shows the distributions of the Vessel Area Density (VAD) across the four feature sets:

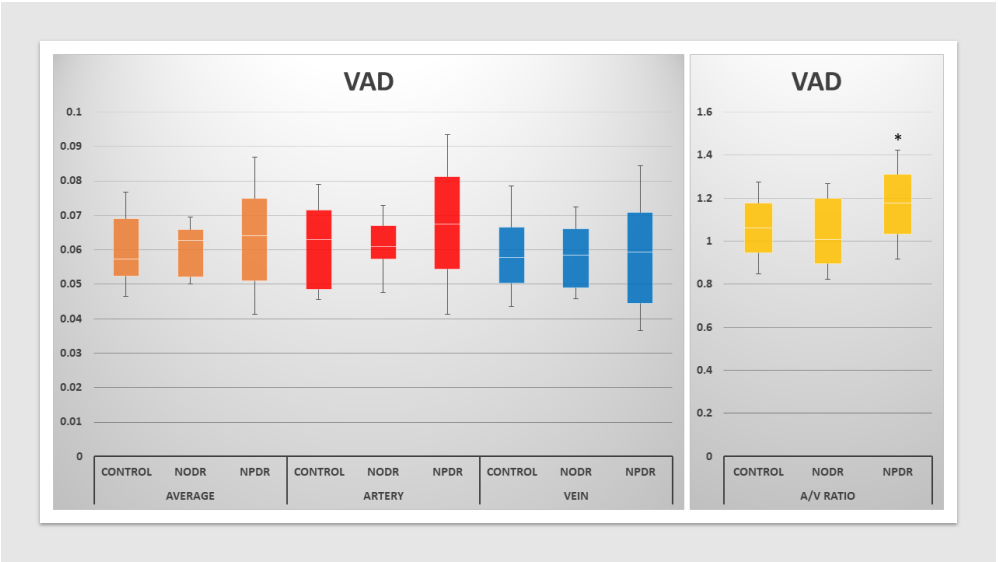


Figure 3.4: VAD Box and Whisker Plot

As can be seen, this feature seems to be useful only in the A/V Ratio measurements. The NPDR distribution can be distinguished from the others.

### 3.3.5 VCI Box and Whisker Plot

The next graph shows the distributions of the Vessel Complexity Index (VCI) across the four feature sets:

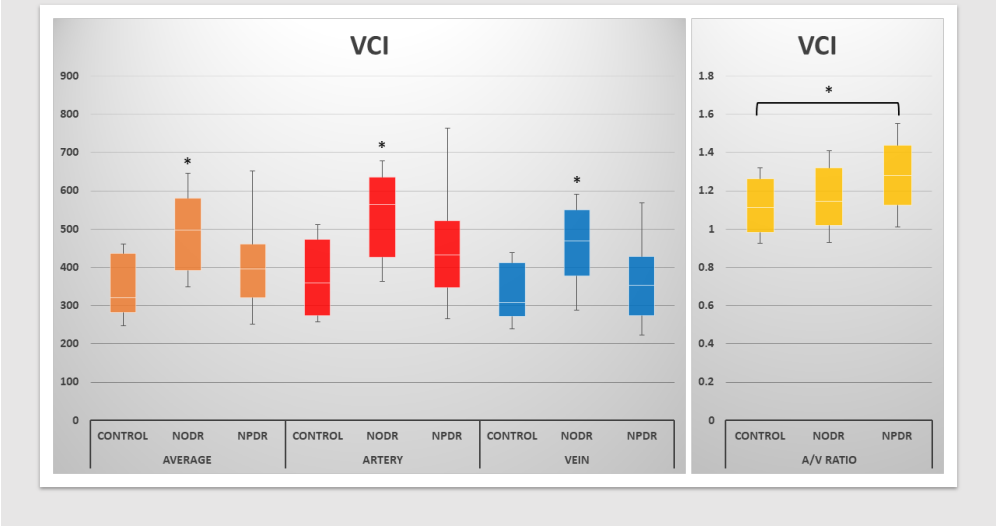


Figure 3.5: VCI Box and Whisker Plot

As can be seen, the NoDR distributions follow the same trend as in VAD, while the A/V Ratio measurements follow an ascending trend.

### 3.3.6 FD Box and Whisker Plot

The next graph shows the distributions of the Fractal Dimension (FD) across the four feature sets:

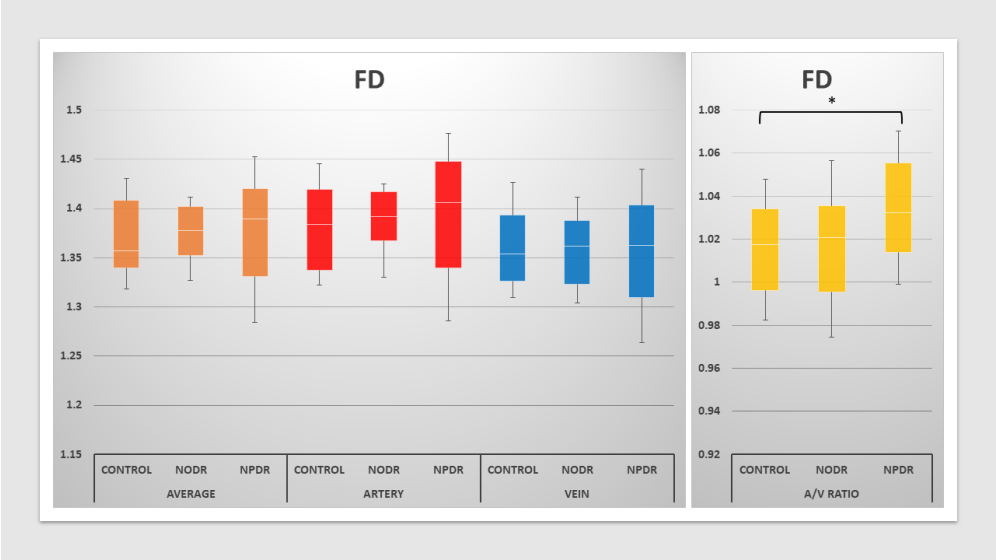


Figure 3.6: FD Box and Whisker Plot

As can be seen, the A/V Ratio distributions follow the trend seen in VCI, where the NPDR values rise over the two other distributions but are significantly different only from the Control cohort.

## 3.4 Second Kruskal-Wallis Tests

These tests were performed in order to see whether the Mild, Moderate and Severe NPDR have statistically different distributions. A summary of the distribution of the features for the three cohorts and their p-values are shown in the next tables.

### 3.4.1 Artery Features

The following table shows the median values values and the 25th and 75th percentiles of the distributions of the cohorts, alongside the Kruskal-Wallis p-value, for the features measured on the Artery Vessel Maps:

| Features | Mild NPDR | Moderate NPDR | Severe NPDR | p-values |
|---|---|---|---|---|
| **VPI** | 0.060 (0.050-0.069) | 0.056 (0.047-0.070) | 0.066 (0.045-0.075) | 0.5599 |
| **VDI** | 2.459 (2.379-2.498) | 2.560 (2.466-2.711) | 2.725 (2.547-2.900) | **<0.0001** |
| **VSD** | 0.026 (0.022-0.029) | 0.024 (0.020-0.029) | 0.027 (0.018-0.032) | 0.6737 |
| **VAD** | 0.064 (0.053-0.074) | 0.060 (0.051-0.077) | 0.074 (0.058-0.082) | 0.2712 |
| **VCI** | 421.6 (344.1-470.4) | 417.0 (346.6-502.9) | 472.5 (357.2-531.4) | 0.3679 |
| **FD** | 1.403 (1.363-1.433) | 1.397 (1.341-1.430) | 1.425 (1.329-1.449) | 0.6005 |

Table 3.8: Distributions and p-values of the Artery Features.

Based on the p-values, it can be asserted that only VDI is able to differentiate at least one stage of the illness from the other two.

### 3.4.2 Vein Features

The following table shows the median values values and the 25th and 75th percentiles of the distributions of the cohorts, alongside the Kruskal-Wallis p-value, for the features measured on the Vein Vessel Maps:

| Features | Mild NPDR | Moderate NPDR | Severe NPDR | p-values |
|---|---|---|---|---|
| **VPI** | 0.052 (0.039-0.063) | 0.047 (0.039-0.055) | 0.053 (0.044-0.059) | 0.4819 |
| **VDI** | 2.580 (2.543-2.661) | 2.703 (2.614-2.884) | 2.904 (2.775-3.065) | **<0.0001** |
| **VSD** | 0.022 (0.016-0.027) | 0.019 (0.016-0.023) | 0.021 (0.018-0.025) | 0.4561 |
| **VAD** | 0.058 (0.041-0.073) | 0.051 (0.045-0.061) | 0.063 (0.054-0.071) | 0.2865 |
| **VCI** | 352.9 (266.7-423.2) | 326.3 (277.9-390.2) | 364.8 (296.7-480.0) | 0.3642 |
| **FD** | 1.365 (1.302-1.412) | 1.335 (1.309-1.375) | 1.371 (1.318-1.403) | 0.3716 |

Table 3.9: Distributions and p-values of the Vein Features.

Based on the p-values, it can be asserted that,as before, VDI seems capable of separating at lest one of the cohorts from the other two.

### 3.4.3 A/V Differential Features

The following table shows the median values values and the 25th and 75th percentiles of the distributions of the cohorts, alongside the Kruskal-Wallis p-value, for the ratios of the features measured on the Artery Vessel Maps and the ones measured on the Vein Vessel Maps:

| Features | Mild NPDR | Moderate NPDR | Severe NPDR | p-values |
|---|---|---|---|---|
| **VPI** | 1.187 (1.044-1.415) | 1.210 (1.122-1.292) | 1.258 (1.093-1.409) | 0.7371 |
| **VDI** | 0.935 (0.910-0.963) | 0.943 (0.924-0.964) | 0.927 (0.904-0.984) | 0.2837 |
| **VSD** | 1.212 (1.045-1.465) | 1.223 (1.126-1.308) | 1.270 (1.085-1.450) | 0.8395 |
| **VAD** | 1.139 (0.987-1.350) | 1.170 (1.072-1.256) | 1.186 (1.006-1.325) | 0.8437 |
| **VCI** | 1.248 (1.093-1.422) | 1.227 (1.170-1.360) | 1.352 (1.088-1.473) | 0.5220 |
| **FD** | 1.029 (1.010-1.063) | 1.029 (1.018-1.044) | 1.037 (1.013-1.062) | 0.7558 |

Table 3.10: Distributions and p-values of the A/V Differential Features.

Based on the p-values, it can be asserted that none of these A/V Ratio features seems able to differentiate between the three stages of the illness. This might also mean that the changes in the values of the Artery and Vein features due to the onset and the worsening of NPDR may happen with the same ratio.

### 3.4.4 Average Features

The following table shows the median values values and the 25th and 75th percentiles of the distributions of the cohorts, alongside the Kruskal-Wallis p-value, for the averages of the features measured on the Artery Vessel Maps and the Vein Vessel Maps:

| Features | Mild NPDR | Moderate NPDR | Severe NPDR | p-values |
|---|---|---|---|---|
| **VPI** | 0.058 (0.044-0.066) | 0.052 (0.044-0.063) | 0.061 (0.047-0.066) | 0.4991 |
| **VDI** | 2.517 (2.476-2.552) | 2.645 (2.529-2.765) | 2.813 (2.650-2.941) | **<0.0001** |
| **VSD** | 0.025 (0.020-0.028) | 0.021 (0.018-0.026) | 0.025 (0.019-0.028) | 0.5827 |
| **VAD** | 0.062 (0.048-0.075) | 0.055 (0.048-0.070) | 0.069 (0.055-0.076) | 0.2541 |
| **VCI** | 397.9 (296.9-439.1) | 368.8 (313.5-432.5) | 418.4 (360.5-481.2) | 0.3679 |
| **FD** | 1.392 (1.334-1.422) | 1.364 (1.326-1.398) | 1.402 (1.335-1.421) | 0.4795 |

Table 3.11: Distributions and p-values of the Average Features.

As expected, based on VDI's Artery and Vein p-values, it can be seen how the Average VDI distributions contain at least one that is significantly different from the others.

## 3.5 Second Mann-Whitney Tests

After these last Kruskal-Wallis tests, only VDI can be identified as a promising feature. As seen before, a series of three Mann-Whitney statistical testsare perfomed in order to see which cohorts can be separated from each other. The three tests are:

- Mild NPDR vs Moderate NPDR
- Mild NPDR vs Severe NPDR
- Moderate NPDR vs Severe NPDR

As before, the Bonferroni Correction will be applied. So, p-values that do not pass the new significance threshold but are still lower than the original threshold will be still marked with the * symbol, while the p-values that pass the new significance threshold will be shown in bold.

### 3.5.1 VDI's Mann-Whitney Tests

In the next table, the p-values for all three Mann-Whitney test performed on VDI's values are shown:

| p-values | Mild vs Moderate | Mild vs Severe | Moderate vs Severe |
|---|---|---|---|
| **Artery** | **0.0061** | **<0.0001** | 0.0324* |
| **Vein** | **0.0061** | **<0.0001** | **0.0135** |
| **A/V Ratio** | 0.2585 | 0.7795 | 0.1211 |
| **Average** | **0.0039** | **<0.0001** | **0.0114** |

Table 3.12: p-values of VDI's Mann-Whitney tests.

As can be seen, Average features seem to be better than individual Artery and Vein features in separating the cohorts. The last feature set, along with the Vein only measurements, seems to be able to distinguish all three stages of NPDR from each other, with a greater confidence in separating Mild NPDR from Severe NPDR.

### 3.5.2 VDI NPDR Box and Whisker Plot

To better visualize the differences and similarities between the distributions of VDI in the three stages of NPDR, a box and whisker plot is shown in this section. As before, a distribution is marked if it is significantly different from the other two or only one of the other distributions. Only p-values that passed the Bonferroni Correction were used.

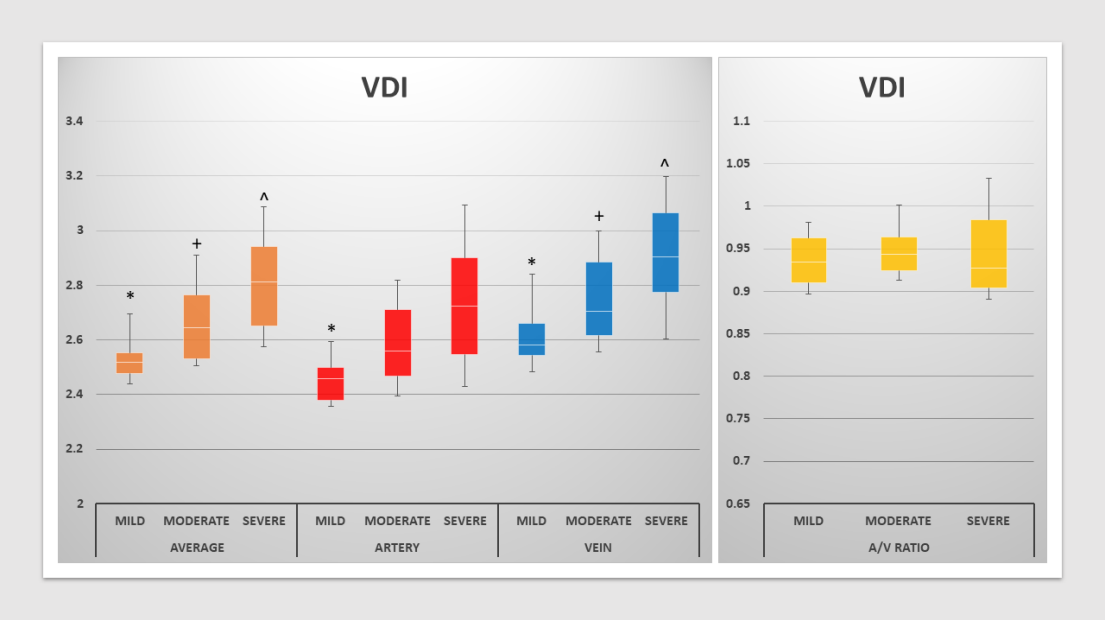


Figure 3.7: FD Box and Whisker Plot

A very clear ascending trend can be seen. While the Artery distributions closer together, the Vein and Average ones can be each separated from the others. The distributions of the A/V Ratios are similar and thus not differentiable, as seen in Table 3.10.

In the next chapter, these results will be discussed and compared to previous findings of similar studies.

# Chapter 4

# Discussion

To summarize, vessels found in OCTA images were differentiated into arteries and veins by an automatic procedure. After this, another automatic procedure was used to measure and extract six features (VPI, VDI, VSD, VAD, VCI and FD). Two rounds of statistical tests were performed on two sets of three different cohorts in order to see which distributions were significantly different from the others.

## 4.1 Discussion about the Distributions of the Features

The previously shown results will be discussed, for every feature, in the following sections. These results will be compared to previous findings of similar studies.

### 4.1.1 VPI

The Vessel Perimeter Index, which is calculated with Equation 2.1, represents the share of pixels in the image that sit on the vessels diameters. It was chosen because VPI "can detect abnormal microvasculature and also provide repeatable quantitative results" [35].

In this study, VPI was found to be most significant if measured by taking A/V Ratios (Table 3.3). In this way, this feature seems to be able to differentiate the Control and NoDR patients from the NPDR ones (Tables 3.6 and 3.7), while being unable to tell these first two cohorts apart (Table 3.5).

While, with the other measurement modalities, VPI shows a somewhat ascending trend, with A/V Ratios it shows a clear spike for NPDR values (Figure 3.1). This might happen because the illness affects arteries and vein in a different way. Remembering the formula for VPI calculation, NPDR seems to be the cause

of an increase in perimeter pixels in arteries, while seeming to not cause similar changes in veins. Also, looking at the Artery distributions, it can be seen that there seem to be significantly more perimeter pixels in images of NPDR patients compared to images of NoDR patients.

According to measurements made by Chu et al. on Optical Microangiography (OMAG) OCTA images, [35], VPI was found to decrease with the presence of the illness. VPI was also found to decrease in Sickle Cell Retinopathy [21]. In this study, however, it seems to not follow these global trend. Perhaps this discrepancy is due to the measurement modalities, which did not include unclassified vessel maps. Perhaps, differentiating Arteries from Veins has a more complex influence on the measuring process.

### 4.1.2 VDI

The Vessel Diameter Index, which is calculated with Equation 2.2, represents the average diameter of all the vessels in the image. In this study, VDI was the only feature to not show a significant p-value in the A/V Ratio measurements (Table 3.3). Conversely, it seems able to differentiate Control and NPDR patients from the NoDR ones (Tables 3.5 and 3.7). This separation seems to be clearer in the Vein measurements.

The NoDR distribution can be distinguished based on the fact that its values are broadly higher than the ones in the other two cohorts, as seen in Figure 3.2. Remembering the formula for VDI calculation, NoDR patients seem to suffer from an increase in area of the vessels and/or a decrease in their skeleton pixels (total length of the vessels). The distributions of Vessel Skeleton Density and Vessel Area Density should help us to better understand the balance of these two effects. Since the A/V Ratio distributions do not seem to be significantly different from one another, it can be stated that the equilibrium between VDI in Arteries and Vein seems to be maintained.

VDI is also the only feature in this study that seems to be able to differentiate between all three NPDR cohorts (Table 3.12). As seen in Figure 3.7, Averaged VDI values (like Artery and Vein ones), show a very clear ascending trend between the cohorts, with the Mild NPDR distribution being quite compact. A static A/V Ratio trend suggests that the relationships between Artery and Vein VDIs are conserved in all stages of NPDR. Taking into account the A/V Ratio information from before, it can be observed how A/V Ratio VDI values seem to be consistent among all distributions.

Chu et al. found that VDI increased in NPDR patients [35]. A significant VDI increase was measured between Control and Severe NPDR patients in Superficial Layer OCTA by Kim et al [36], who also observed a positive correlation between VDI and Diabetic Retinopathy Severity. This positive correlation can be found in this study in Figure 3.7. Healthy eyes could not be differentiated from Mild

NPDR eyes. Frizziero et al. measured VDI in ring-shaped regions of interest in OCTA images and observed a significant decrease of the feature in Mild and Moderate NPDR patients compared to the Control cohort [37]. These levels of significance were not found in Severe NPDR eyes. It was also observed that "larger peripapillary vessels showed a significant increase in VDI in NPDR eyes." The behaviour of VDI in NPDR does not seem to be universal. Moreover, since the NoDR cohort was not included in these cited studies, the spike in VDI observed in NoDR patients in this study could not be reported.

### 4.1.3 VSD

The Vessel Skeleton Density, which is calculated with Equation 2.3, represents the share of skeleton pixels in the image. In other words, it is a measure of the combined lengths of the vessels in the image. In this study, VSD was found to be most significant if measured by taking A/V Ratios. In this way, this feature seems to be able to differentiate the Control patients from the NPDR ones (Table 3.6), while not managing to show a significant p-value after the Bonferroni Correction in the NoDR vs NPDR cohorts test (Table 3.7).

As can be observed in Figure 3.3, VSD shows a very weak increasing trend for Artery and Average values, but it also shows a very weak decreasing trend for the values measured on Vein maps. These two seemingly weak trends have a combined effect in the A/V Ratio measurements. As can be seen in their distributions, values from NPDR patients experience a bump such as their distribution can told apart from the Control patients cohort. Thus, it seems that the slight increase in Arteries and the slight decrease in Veins of VSD makes their ratios a useful measure to describe what appears to be a disequilibrium.

Chu et al observed an increase in VSD between Control and NPDR patients [35]. This trend is weakened in this study's Averaged distributions, which are closer to a measurement on an unclassified image. Kim et al., however, found a significant VSD decrease between Control patients and both Mild and Severe NPDR cohorts, demonstrating a negative correlation with the severity of the illness. Durbin et al. also observed a negative correlation between VSD and severity of Diabetic Retinopathy (and also age of the subject) [38]. Khadamy et al. found a significantly lower VSD among DR patients compared to Healthy ones [28]. In this study, a very weak version of both trends can be observed in Arteries and Veins. However, apart from A/V Ratio, no VSD distributions are statistically different from the others.

### 4.1.4 VAD

The Vessel Area Density, which is calculated with Equation 2.4, represents the share of area pixels in the image. In other words, it is a measure of the combined areas of the vessels in the image. It was chosen also because it strongly correlates with FAZ Area and FAZ Acircularity [34]. In this study, VAD was found to be most significant if measured by taking A/V Ratios (Table 3.3). Like VPI, this feature seems to be able to differentiate the Control and NoDR patients from the NPDR ones (Tables 3.6 and 3.7), while being unable to tell these first two cohorts apart (Table 3.5).

As can be observed in Figure 3.4, VAD shows a very weak increasing trend for Artery and Average values, while not showing a particular trend for the values measured on Vein maps. As can be seen in their A/V Ratio distributions, values from NPDR patients experience a bump such as their distribution can told apart from the Control and NoDR patients cohorts. Thus, it seems that also NPDR VAD A/V Ratios suggest a disequilibrium that does not occur in patients with Diabetes alone. Remembering the formula for VAD calculation, it is clear that any differences in distributions are due to a significant increase or decrease of the total vessel area in the image. In case of A/V Ratios, a significant increase in NPDR VAD values means that the area of arteries increased and/or the area of veins decreased. Thus latter case does not seem to be happening, since Vein distributions are observed to be indistinguishable from each other (Table 3.2). In fact, measurements from VPI, VSD, VDI and VAD seem to suggest that vein microvasculature is affected by NPDR in a minor way compared to arteries.

Chu et al observed that VAD decreases in NPDR patients, but "has the complication of not changing when there are decreased perfusion and vessel dilation happening at the same time" [35]. This fact might explain the weak or absent trends in VAD distributions. Moreover, since in that study there was no NoDR cohorts, some of those changes could have been introduced by Diabetes. The bump in A/V Ratio NPDR values might thus be interpreted as an imbalance between decreasing perfusion and vessel dilation in arteries and veins. The latter component seems to beat the former in artery measurements, causing a significant increase in A/V Ratios.

Kim et al also found a significant decrease in VAD from Control to NPDR patients [36]. This decrease slowed when Severe NPDR becomes PDR. However, Hyungwoo et al observed an increase in VAD when NPDR approaches PDR [34]. Frizziero et al also found VAD to be "significantly reduced in NPDR eyes, along with the progression of NPDR" [37]. In his review, Tey et al assert that "vessel density decreases in a patient with DR, as well as a diabetic patient without DR, attributing to the fact that parafoveal capillary nonperfusion may potentially be an early sign of DR" and that "despite the contradictory results, VAD has shown to decrease in DR" [27]. The absence of a descending trend in this study might be explained by the work by Khadamy et al, which state that "Repeated VD

measurements using the same device is reliable; however, significant variability exists in measurements using different devices and methods. Hence, comparisons should be made using the same type of device.". Also, it states that VAD is correlated with age and sex but not with HbA1c or duration of Diabetes. Thus, it can be seen that there are many variables at play behind this simple feature, and a direct comparisons may not be so informative.

### 4.1.5 VCI

The Vessel Complexity Index, which is calculated with Equation 2.5, represents the visual complexity of the pattern of the vessels. In this study, VCI was found to be the feature with most significant p-values, achieving statistical significance in every feature set (Tables 3.1 to 3.4). In the Artery, Vein and Average measurements, the NoDR distribution can be differentiated from the other Control and NPDR patients. In A/V Ratio measurements, the NPDR cohorts can be differentiated only from the Control one.

As can be observed in Figure 3.5, VCI values show a triangle-shaped trend. Looking at the A/V Ratio distributions, there seems to be an ascending trend. There seem to be a growing imbalance between Artery and Vein VCI that starts in patients with Diabetes and increases in patients with NPDR. Remembering the formula for VCI calculation, it is clear that understanding the underlying causes of such changes might not be so straightforward. However, the previous features could be used to help this explanation, namely VPI and VAD, which depend only on one of the terms which compose VCI. It is also worth remembering that squaring the perimeter pixels in the numerator makes the relationship between VCI and these two features non-linear.

Chu et al [35] introduced this parameter as a microvasculature feature for the first time in 2016, observing a decrease in VCI between Control and DR patients. Vessel Complexity Index was reported to be able to distinguish between NPDR and PDR patients by Alam et al [39]. Neither of these studies have tested VCI on a NoDR cohort. VCI seems to be most useful when a significant difference in visual complexity of the vasculature occurs.

### 4.1.6 FD

The Fractal Dimension, which is calculated with the Box-Counting method, is associated with visual complexity and vessel tortuosity. In this study, FD was found to be the worst performing feature in this study. In A/V Ratio measurements, the NPDR cohorts can be differentiated only from the Control one (Table 3.6). Its Vein distributions are almost the same for the three cohorts (Table 3.2). Its Artery and Average distributions seem to follow a very weak ascending trend

(Figure 3.6). Perhaps this is why a significant increase from Control values to NPDR values in the FD A/V Ratio distributions.

Kim et al observed that "FD progressively decreased with increasing severity of DR" [36], suggesting a gradual loss of vessel complexity. Zahid et al also found that FD decreases in eyes affected by DR [41]. However, calculating the Fractal Dimension using the Box-Counting method implies that its Artery and Vein (and, by extension, Average and A/V Ratio) values are quite different from the values that could be measured on an undifferentiated vessel map. This has the upside of exploring new ways of DR identification, but has the downside of not being comparable to previous measurements (which used unclassified images).

## 4.2 Insights given by the Significant Differences in Value Distributions

In this section, all the significant differences that have arisen from the statistical tests are put together to gain insights about the changes on microvasculature properties caused by the presence of Diabetes Mellitus and then Non-Proliferative Diabetic Retinopathy.

The value distributions of VPI seem to give us the following insights:

- The number of vessel perimeters pixels of arteries increases when, starting from a condition of Diabetes Mellitus, NPDR develops in the eye. This increase is more contained between Healthy and NPDR eyes.
- NPDR eyes have a higher A/V Ratio concerning the vessel pixels than the other two cohorts. This seems to be caused by an increase of Artery values rather than a decrease in Vein values.
- NPDR stages are not differentiable between themselves based only on vessel perimeter pixels. In the A/V Ratio case, this could mean that a certain Artery-Vein balance, which seems only slightly perturbed by Diabetes, is being dragged towards a higher equilibrium point, which identifies all stages of NPDR. This balance must be linked to the effects of the illness on the microvasculature of the eyes.

The value distributions of VDI seem to give us the following insights:

- Both in arteries and veins, average vessel diameter values soar in patients affected by Diabetes Mellitus. This is perhaps the result of vessel swelling and blockages.

- A/V Ratio distributions seem to show a weak decrease in values between Control patients and the other two cohorts. This seem to point out a shifted balance caused by Diabetes Mellitus, which is the common trait between the NoDR and NPDR cohorts.
- VDI is able to differentiate between the three stages of NPDR with Artery, Vein and Average measurements. This significant ascending trend is also found in literature, and has to be due to the vessel swelling caused by DR. Since the A/V Ratio distributions of NPDR stages cannot be differentiated, we can assert that, in case of VDI, differentiating Arteries from Veins seems to produce the same results as using unclassified vessel maps.

The value distributions of VSD seem to give us the following insights:

- Due to a somewhat increased number of Artery skeleton pixels and a somewhat decreased number of Vein skeleton pixels, Control patients' A/V Ratio values are observed to be lower than the ones from their NPDR counterparts. This may suggest an alteration of balance due to the opposite effect that NPDR seems to have on the two classes of vessels.

The value distributions of VAD seem to give us the following insights:

- A/V Ratio NPDR value are significantly higher than both Control and NoDR ones. This suggests an imbalance due to the presence of NPDR.
- While Vein distributions are totally indistinguishable from each other, Artery NPDR values are slightly higher. This fact seems to suggest that DR could be effecting arteries more than veins.
- Coupling this information with the ones from VSD, it is clear that VDI Control and NPDR values seems similar because both skeleton and area pixels slightly rise in arteries while they remain the same in veins. Also, observing the NoDR distributions in VSD and VAD, it is clear how the VDI ones result higher than the other two cohorts: the skeleton pixels are on the lower side, while the area pixels are on par with the Control cohort.
- Looking at the VDI Vein NPDR distribution, it can be seen that it seems slightly higher that its Control counterpart. However, their area pixel (VAD) distributions seem exactly the same. A sightly higher average diameter but the same vessel area can be explained by the contemporary swelling and blockages of the veins, condition described by Chu et al [35].

The value distributions of VCI seem to give us the following insights:

- Both in arteries and veins, average vessel diameter values soar in patients affected by Diabetes Mellitus. This increased vessel visual complexity can be the effects of many causes.
- On the A/V Ratio front, VCI seems to be able to differentiate the Control and the NPDR patients, with the NoDR distribution being observed as some kind of a middle point. This could be interpreted as a continuous process that steers the artery-vein equilibrium from one point to another. The higher NoDR values are thus still following this equilibrium path.
- Once this trend is ascertained, the causes can be at most two: the increase in complexity of Arteries and/or the loss of complexity of Veins. Looking at the Artery and Vein Control and NPDR distributions, the latter hypothesis can be excluded. Thus, an increases Artery visual complexity (relative to the Veins' one) is possibly the cause of this trend.
- This means that, in Veins, number of perimeter (VPI) and area (VAD) pixels should stay similar to the Control case. Also, Artery VPI and VAD NPDR values seem to be slightly higher than Control ones. However, since the number of perimeter pixels is squared at the numerator in order to calculate VCI, these changes should determine the increase in Artery complexity. All these conditions are verified in this study.

The value distributions of FD seem to give us the following insights:

- A/V Ratio NPDR values rise significantly above their Control counterparts, and almost significantly above their NoDR counterparts. This seems to point at an effect of Diabetic Retinopathy. This effect has to be due to an increase in Artery complexity and tortuosity, and/or a decrease in these properties of Veins. The latter cause is to exclude, while the former is likely the prime cause of these changes. This reasoning is also supported by observations of increased in visual complexity in arteries in VCI.

# Conclusions

To summarize, measuring previously established features on differentiated artery-vein OCTA vessel maps in order to identify Non-Proliferative Diabetic Retinopathy has produced helpful and insightful results.

Measuring the features on arteries and veins only is not an improvement per se. It is however very important because it enables the calculation of the A/V Ratios. These have been shown to be a high-significance type of measurement: of the six features, five have statistically different distributions among their cohorts. In this study, A/V Ratios have shown the potential to differentiate NPDR patients from at least one between the Control and the NoDR cohorts. In the case of VPI and VAD the NPDR values can be differentiated from both the other two cohorts. A/V Ratio measurements have also been devised to take advantages of the imbalances between artery and vein values, thus showing a difference in effect and/or magnitude of effect of the illness. In light of this, it is possible to say that, in five out of the six analyzed features, NPDR introduces a perturbation in the equilibrium that seems to be in place between arteries and veins values. This effect is now quantifiable and is able to be used to gain more insights on and to better identify the first stages of DR, which have been established to be the most crucial regarding diagnosis. The fact that this type of measurement does not seem able to distinguish between the three NPDR cohorts further validate this hypothesis, since the changes introduced by the onset of DR are maintained throughout NPDR stages.

An interesting finding is the high significance of VCI in all of its measurements. The Vessel Complexity Index is a feature that has had minor attention in literature. However, in this study, it has shown a great potential. Incorporating vessel perimeter and area information into a unique parameter seems to result in a perceivable increase in significance. Perhaps, VCI will be studied further in future research.

Of the six features, only one seems able to differentiate between the three stages of NPDR: the Vessel Diameter Index. This feature shows a very clear ascending trend and can differentiate every NPDR cohort from each other. This could be a very important finding, since, once NPDR is diagnosed, its staging could be also done automatically in a more easier fashion.

# Bibliography


[1] Engelgau M.M. Geiss L.S. Saaddine J.B. et al. The Evolving Diabetes Burden in the United States. *Annals of Internal Medicine*, 140:945–950, 2004.

[2] Kempen J.H. O'Colmain B.J. Leske M.C. Haffner S.M. Klein R. Moss S.E. Taylor H.R. Hamman R.F. West S.K. Wang J.J. Congdon N.G. and Friedman D.S. The Prevalence of Diabetic Retinopathy among Adults in the United States. *Archives of ophthalmology*, 122(4):552–563, 2004.

[3] Pandey S.K. Sharma V. World diabetes day 2018: Battling the Emerging Epidemic of Diabetic Retinopathy. *Indian Journal of Ophthalmology*, 66(11):1652–1653, 2018.

[4] Murray C.D. The Physiological Principle of Minimum Work: I. The Vascular System and the Cost of Blood Volume. *Proceedings of the National Academy of Sciences of the United States of America*, 12(3):207–214, 1926.

[5] Ernest J.T. Goldstick T.K. Engerman R.L. Hyperglycemia impairs retinal oxygen autoregulation in normal and diabetic dogs. *Investigative Ophthalmology and Visual Science*, 24(7):985–989, 1983.

[6] Grunwald J.E. DuPont J. Riva C.E. Retinal haemodynamics in patients with early diabetes mellitus. *The British Journal of Ophthalmology*, 80(4):327–331, 1996.

[7] Sasongko M.B. Wang J.J. Donaghue K.C. et al. Alterations in retinal microvascular geometry in young type 1 diabetes. *Diabetes Care*, 33(6):1331–1336, 2010.

[8] Saine P.J. and Tyler M.E. *Ophthalmic Photography: Retinal Photography, Angiography, and Electronic Imaging, 2nd Edition*. Butterworth-Heinemann Medical, 2002.

[9] Castelnuovo M. Differential Artery-Vein Analysis in OCT Angiography of Diabetic Retinopathy. *Master Thesis, University of Illinois at Chicago*, 2021.

[10] Alam M. Son T. Toslak D. Lim J.I. and Yao X. Combining ODR and Blood Vessel Tracking for Artery- Vein Classification and Analysis in Color Fundus Images. *Translational Vision Science and Technology*, 7(2):23, 2018.

[11] Gupta A. Chhikara R. Diabetic retinopathy: Present and past. *Procedia Computer Science*, 132:1432–1440, 2018.

[12] Habib M.S. Al-Diri B. Hunter A. et al. The association between retinal vascular geometry changes and diabetic retinopathy and their role in prediction of progression – an exploratory study. *BMC Ophthalmology*, 14:89, 2014.

[13] Gao S.S. Jia Y. Zhang M. Su J.P. Liu G. Hwang T.S. Bailey S.T. Huang D. Optical Coherence Tomography Angiography. *Investigative Ophthalmology and Visual Science*, 57(9):27–36, 2016.

[14] Yao X. Alam M. Le D. Toslak D. Quantitative optical coherence tomography angiography: A review. *Experimental Biology and Medicine*, 245:301–312, 2020.

[15] Alam M. Le D. Lim J.I. Chan R.V.P. and Yao X. Unsupervised Machine Learning Based Multi-Task Artificial Intelligence Classification of Retinopathies. *Journal of Clinical Medicine*, 8, 2019.

[16] Arya M. Sabrosa A.S. Duker J.S. Waheed N.K. Choriocapillaris changes in dry age-related macular degeneration and geographic atrophy: a review. *Eye and Vision*, 5(22), 2018.

[17] Perrott-Reynolds R. Cann R. Cronbach N. et al. The diagnostic accuracy of OCT angiography in naive and treated neovascular age-related macular degeneration: a review. *Eye*, 33(2):274–282, 2019.

[18] Moreira-Neto C.A. Moult E.M. Fujimoto J.G. Waheed N.K. Ferrara D. Choriocapillaris Loss in Advanced Age-Related Macular Degeneration. *Journal of Ophthalmology*, 2018.

[19] Usman M. Iqbal K. Ali M.H. Nafees K. Features and Diagnostic Accuracy of Optical Coherence Tomography Angiography in Neovascular Age-related Macular Degeneration. *Cureus*, 11(12), 2019.

[20] Arrigo A. Aragona E. Bordato A. et al. Quantitative OCTA parameter variations after treatment of macular neovascularization secondary to age-related macular degeneration. *Retina*, 2020.

[21] Alam M. Thapa D. Lim J.I. Cao D. Yao X. Quantitative characteristics of sickle cell retinopathy in optical coherence tomography angiography. *Biomedical Optics Express*, 8(3):1741:1753, 2017.

[22] Alam M. Lim J.I. Toslak D. Yao X. Differential Artery–Vein Analysis Improves the Performance of OCTA Staging of Sickle Cell Retinopathy. *Translational Vision Science and Technology*, 8(2):3, 2019.

[23] Sambhav K. Grover S. Chalam K.V. Temporal Thinning In Sickle Cell Retinopathy Is Associated With Diminished Perfusion On Octa And Dense Scotoma On Microperimetery. *Retinal Cases and Brief Reports*, 13(4):308–313, 2019.

[24] Grego L. Pignatto S. Alfier F. et al. Optical coherence tomography (OCT) and OCT angiography allow early identification of sickle cell maculopathy in children and correlate it with systemic risk factors. *Graefe's Archive for Clinical and Experimental Ophthalmology*, 258:2551–2561, 2020.

[25] Le D. Alam M. Miao B.A. Lim J.I. Yao X. Fully automated geometric feature analysis in optical coherence tomography angiography for objective classification of diabetic retinopathy. *Biomedical Optics Express*, 10(5):2493–2503, 2019.

[26] Eladawi N. Elmogy M. Khalifa F. Ghazal M. Ghazi N. Aboelfetouh A. Riad A. Sandhu H. Schaal S. and El-Baz A. Early diabetic retinopathy diagnosis based on local retinal blood vessel analysis in optical coherence tomography angiography (OCTA) images. *Medical Physics*, 45:4582–4599, 2018.

[27] Tey K.Y. Teo K. Tan A.C.S. et al. Optical coherence tomography angiography in diabetic retinopathy: a review of current applications. *Eye and Vision*, 6(37), 2019.

[28] Khadamy J. Abri Aghdam K. Falavarjani K.G. An Update on Optical Coherence Tomography Angiography in Diabetic Retinopathy. *Journal of Ophthalmic and Vision Research*, 13(4):487–497, 2018.

[29] Alonso-Plasencia M. Abreu-González R. Gómez-Culebras M.A. Structure-Function Correlation Using OCT Angiography And Microperimetry In Diabetic Retinopathy. *Clinical Ophthalmology*, 13:2181–2188, 2019.

[30] Cano J. O'neill W.D. Penn R.D. et al. Classification of advanced and early stages of diabetic retinopathy from non-diabetic subjects by an ordinary least squares modeling method applied to OCTA images. *Biomedical Optics Express*, 11(8):4666–4678, 2020.

[31] Alam M. Zhang Y. Lim J.I. Chan R.V.P. Yang M. and Yao X. Quantitative Optical Coherence Tomography Angiography Features for Objective Classification and Staging of Diabetic Retinopathy. *Retina*, 40:322–332, 2020.

[32] Hsieh Y.T. Alam M. Le D. Hsiao C.C. Yang C.H. Chao D.L. and Yao X. OCT Angiography Biomarkers for Predicting Visual Outcomes after Ranibizumab Treatment for Diabetic Macular Edema. *Retina*, 3(10):826–834, 2019.

[33] Le D. Alam M. Yao C.K. Lim J.I. Hsieh Y.T. Chan R.V.P. Toslak D. and Yao X. Transfer Learning for Automated OCTA Detection of Diabetic Retinopathy. *Translational Vision Science and Technology*, 9(2):35, 2020.

[34] Lee H. Lee M. Chung H. Kim H.C. QUANTIFICATION OF RETINAL VESSEL TORTUOSITY IN DIABETIC RETINOPATHY USING OPTICAL COHERENCE TOMOGRAPHY ANGIOGRAPHY. *Retina*, 38(5):976–985, 2018.

[35] Chu Z. Lin J. Gao C. Xin C. Zhang Q. Chen C. Roisman L. Gregori G. Rosenfeld P.J. and Wang R.K. Quantitative assessment of the retinal microvasculature using optical coherence tomography angiography. *Journal of Biomedical Optics*, 21(6), 2016.

[36] Kim A.Y. Chu Z. Shahidzadeh A. Wang R.K. Puliafito C.A. Kashani A.H. Quantifying Microvascular Density and Morphology in Diabetic Retinopathy Using Spectral-Domain Optical Coherence Tomography Angiography. *Investigative Ophthalmology and Visual Science*, 57(9):362–370, 2016.

[37] Frizziero L. Parrozzani R. Londei D. et al. Quantification of vascular and neuronal changes in the peripapillary retinal area secondary to diabetic retinopathy. *British Journal of Ophthalmology*, 2020.

[38] Durbin M.K. An L. Shemonski N.D. Soares M. Santos T. Lopes M. Neves C. Cunha-Vaz J. Quantification of Retinal Microvascular Density in Optical Coherence Tomographic Angiography Images in Diabetic Retinopathy. *Journal of the American Medical Association Ophthalmology*, 135(4):370–376, 2017.

[39] Alam M. Le D. Lim J.I. Yao X. Quantitative analysis of vascular complexity in OCTA of diabetic retinopathy. *Proceedings SPIE Volume 11218, Ophthalmic Technologies XXX*, 2020.

[40] Reif R. Qin J. An L. Zhi Z. Dziennis S. Wang R. Quantifying optical microangiography images obtained from a spectral domain optical coherence tomography system. *International Journal of Biomedical Imaging*, 2012.

[41] Zahid S. Dolz-Marco R. Freund KB. Balaratnasingam C. Dansingani K. Gilani F. Mehta N. Young E. Klifto M.R. Chae B. Yannuzzi L.A. Young J.A. Fractal Dimensional Analysis of Optical Coherence Tomography Angiography in Eyes With Diabetic Retinopathy. *Investigative Ophthalmology and Visual Science*, 57(11):4940–4947, 2016.

[42] Alam M. Toslak D. Lim J.I. and Yao X. Color Fundus Image Guided Artery-Vein Differentiation in Optical Coherence Tomography Angiography. *Investigative Ophthalmology and Visual Sciences*, 59:4953–4962, 2018.

[43] Son T. Alam M. Kim T.H. Liu C. Toslak D. and Yao X. Near infrared oximetry-guided artery-vein classification in optical coherence tomography angiography. *Experimental Biology and Medicine*, 244(10):813–818, 2019.

[44] Alam M. Le D. Son T. Lim J.I. and Yao X. AV-Net: deep learning for fully automated artery-vein classification in optical coherence tomography angiography. *Biomedical Optics Express*, 11:5249–5257, 2020.

[45] Alam M. Toslak D. Lim J.I. and Yao X. OCT feature analysis guided artery-vein differentiation in OCTA. *Biomedical Optics Express*, 10(4):2055–2066, 2019.

[46] Solomon S.D. Chew E. Duh E.J. et al. Diabetic Retinopathy: A Position Statement by the American Diabetes Association. *Diabetes Care*, 40(3):412–418, 2017.

[47] Li C. Xu C. Anderson A.W. and Gore J.C. MRI Tissue Classification and Bias Field Estimation Based on Coherent Local Intensity Clustering: A Unified Energy Minimization Framework. *Information Processing in Medical Imaging*, 5636:288–299, 2009.

[48] Vázquez S.G. Barreira N. Penedo M.G. Saez M. and Pose-Reino A. Using Retinex Image Enhancement to Improve the Artery/Vein Classification in Retinal Images. *Image Analysis and Recognition*, 6612:50–59, 2010.

[49] Bonferroni C.E. Teoria statistica delle classi e calcolo delle probabilità. *Pubblicazioni del Regio Istituto Superiore di Scienze Economiche e Commerciali di Firenze*, 1936.